Title: Organism-wide cellular dynamics and epigenomic remodeling in mammalian aging

Authors: Ziyu Lu[1,2], Zehao Zhang[1,2], Zihan Xu[1,2], Abdulraouf Abdulraouf[1,3], Wei Zhou[1,4*], Junyue Cao[1,4,5*]

Affiliations:
[1]Laboratory of Single Cell Genomics and Population Dynamics, The Rockefeller University, New York, NY, USA
[2]The David Rockefeller Graduate Program in Bioscience, The Rockefeller University, New York, NY, USA
[3]The Tri-Institutional M.D-Ph.D Program, New York, NY, USA
[4]Senior author
[5]Lead Contact
*Correspondence: wzhou@rockefeller.edu (W.Z.), jcao@rockefeller.edu (J.C.)

Abstract:
Aging leads to functional decline across tissues, often accompanied by profound changes in cellular composition and cell-intrinsic molecular states. However, a comprehensive catalog of how the population of individual cell types change with age and the associated epigenomic dynamics is lacking. Here, we constructed a single-cell chromatin accessibility atlas consisting of ~7 million cells from 21 tissue types spanning three age groups in both sexes. This dataset revealed 536 main cell types and 1,828 finer-grained subtypes, defined by unique chromatin accessibility landscapes at ~1.3 million cis-regulatory elements. We observed widespread remodeling of immune lineages, with increases in plasma cells and macrophages, and depletion of T and B cell progenitors. Additionally, non-immune cell populations, including kidney podocytes, ovary granulosa cells, muscle tenocytes and lung aerocytes, showed marked reductions with age. Meanwhile, many subtypes changed synchronously across multiple organs, underscoring the potential influence of systemic inflammatory signals or hormonal cues. At the molecular level, aging was marked by thousands of differentially accessible regions, with the most concordant changes shared across cell types linked to genes related to inflammation or development. Putative upstream factors, such as intrinsic shifts in transcription factor usages and extrinsic cytokine signatures, were identified. Notably, around 40% of aging-associated main cell types and subtypes showed sex-dependent differences, with tens of thousands of chromatin accessibility peaks altered exclusively in one sex. Together, these findings present a comprehensive framework of how aging reshapes the chromatin landscape and cellular composition across diverse tissues, offering a comprehensive resource for understanding the molecular and cellular programs underlying aging and supporting the exploration of targeted therapeutic strategies to address age-related dysfunction.

Main Text:

Introduction:

Aging is the leading risk factor for many diseases, including neurodegenerative disorders, cardiovascular diseases, metabolic conditions, and cancer(*1*). This association underscores the potential of therapies targeting the aging process itself to delay or prevent various age-related diseases, rather than focusing on specific diseases or organs. However, this approach is challenging due to the complexity of aging, which involves widespread changes across various systems and organs (*2*, *3*). Each organ consists of hundreds of unique cellular states with specialized functions, each undergoing varied aging-associated changes. Therefore, a systematic characterization of aging-associated cell states—including their genetic and epigenetic alterations underlying population dynamics—is essential for identifying cellular and molecular targets that could guide the development of targeted therapeutic interventions.

Recent advancements in single-cell genomics have significantly enhanced our ability to map aging-associated cell states. For example, single-cell transcriptomics analyses have enabled us to profile alterations in thousands of genes across millions of cells as they age (*4*–*7*) . However, these analyses typically focus on protein-coding genes and overlook the impact of non-coding genetic elements in regulating cell-type-specific dynamics in aging. Moreover, current single-cell atlas studies often focus on a limited set of organs (*e.g.,* liver, kidney), largely because some other tissues, like the pancreas, are difficult to profile due to high RNA degradation (*8*, *9*). This limitation impedes our ability to assess aging across the entire organism. As a result, we still lack a comprehensive analysis of cell population dynamics and chromatin landscape changes throughout the mammalian body for understanding how non-coding regions, particularly cis-regulatory DNA elements, affect cell states and population dynamics as they age.

Single-cell ATAC-seq(*10*), which analyzes genome-wide chromatin accessibility at the single-cell level, has enabled the mapping of the cell-type-specific chromatin landscape in a range of mammalian tissues(*11*–*14*), aiding in the identification of disease-associated non-coding regions and their corresponding cell types. Among varied scATAC-seq approaches, single-cell ATAC-seq by combinatorial indexing (*sci-ATAC-seq*), allows for high-throughput analysis of tens of thousands of cells from highly heterogeneous tissues in a single experiment(*11*). With a further optimized version of sci-ATAC-seq (EasySci-ATAC), we recently mapped the cell-type-specific chromatin landscape and aging-associated cell population changes in the mammalian brain(*15*). Building on this work, we now extend our analysis beyond a single organ to explore aging-associated changes in cell populations across the entire organism, identifying changes in cellular chromatin states, population dynamics, and associated genetic elements—including cis-regulatory elements and transcription factor motifs—across different ages and sexes.

Results

An organismal, single-cell chromatin accessibility atlas of aging

To map aging-associated cell population dynamics and the cell-type-specific chromatin landscape changes at the organismal scale, we developed an optimized *EasySci-ATAC(15)* protocol that enables high-throughput analysis of mouse tissues across the entire organism (**Methods**). Next we applied this approach to profile 552 samples collected from thirty-two individual mice representing three age groups (1-month, 5-month, and 21-month)(**Table S1**). Each group contained 8-12 sex-balanced biological replicates, except for the female ovary and uterus samples. Twenty-one different tissue types spanning major biological systems were profiled, including the immune system (*i.e.,* bone marrow, spleen, thymus), the cardiovascular system (*i.e.,* heart), the respiratory system (*i.e.,* lung), the digestive system (*i.e.,* liver, pancreas, esophagus, stomach, intestine, cecum, colon), the urinary system (*i.e.,* kidney), the sensory system (*i.e.,* eye), the reproductive system (*i.e.,* ovary/uterus), the musculoskeletal system (*i.e.,* muscle), the integumentary system (*i.e.,* skin), and the adipose tissues, which includes brown adipose tissue (BAT) and white adipose tissues (WAT) in various anatomical locations (*i.e.,* gonadal, inguinal, and mesenteric) (**Fig. 1A**). Of note, the brain was not included here, as it has been extensively analyzed in our previous study(*15*). Also, to enable the investigation of newborn cell dynamics in a companion study, we labeled mice with 5-Ethynyl-2-deoxyuridine (EdU) before tissue collection, similar to our previous work (*16*). This allowed single-cell chromatin accessibility profiling of both sorted DAPI singlets ('all' cells, this study) and EdU+ nuclei ('newborn' cells, analyzed in the companion study) from the same set of samples.

The extracted nuclei from each tissue sample were sorted and combinatorial barcoded through indexed tagmentation, indexed ligation, and indexed PCR (**Fig. 1A**). The resulting libraries were sequenced on the Illumina NovaSeq 6000 system, yielding a total of 95 billion paired-end raw reads. After filtering out low-quality cells and doublets similar to our previous study (*15*) (**Fig. S1A**), we obtained chromatin accessibility profiles for a total of 10,956,311 single cells, including 6,839,086 DAPI singlets and 4,117,225 cells gated on EdU positivity (**Fig. 1B and Fig. S1B**). The median number of cells recovered per tissue range from 115,060 in the esophagus to 1,173,739 in the kidney (**Fig. 1B**). With a low sequencing duplication rate of only 20.1%, we detected a median of 3,031 unique ATAC-seq fragments per nucleus. On average, 29.8% of reads mapped to promoter regions (within ±1 kb of the transcription start site, TSS), aligning with performances from previous single-cell ATAC-seq studies (*11*, *15*) (**Fig. S1C and S1D**). Also, the pseudo bulk ATAC-seq profiles are clustered by tissue type rather than by individual mice, indicating the low technical batch effect across individuals (**Fig. S1E**).

Next, we identified and annotated heterogeneous cell types within each tissue. Applying *SnapATAC2(17)*, we performed dimensionality reduction and Leiden clustering, and manually curated the annotation based on the gene accessibility of known markers (**Table S2, Fig. S2**). Of note, we utilized the full dataset containing 10,956,311 cells for clustering and annotations. Chromatin accessibility alone enabled the identification of diverse cell types, including tissues that are challenging to profile by scRNA-seq due to high RNase levels, such as ductal cells (marked by *Ccn2*), beta-cells (marked by *Gcg*), alpha-cells (marked by *Isn1*) and delta-cells (marked by *Sst*) in the pancreas (*18*, *19*) (**Fig. S2A)**. In total, we annotated 536 organ-level main cell types, which were consolidated into 144 unique categories, with a median of 25 cell types per tissue and 4,860 nuclei per cell type (**Fig. 1C**). While most cell types were restricted to one organ (n = 102), we identified eighteen broadly distributed cell types shared by more than ten tissues, including immune cells (*e.g.,* T cells, B cells), stromal cells (*e.g.,* fibroblasts, smooth muscle cells) and endothelial cells (*e.g.,* vascular and lymphatic endothelial cells).

To globally characterize the cell-type-specific chromatin accessibility landscape, we combined reads from cells of the same type and same tissue, performed peak calling, and iteratively merged the resulting peaks to a universal set of 1,341,077 open chromatin regions (±250 base pairs from peak summit; **Methods**). The genomic distribution of these peaks was largely consistent with previous sn-ATAC-seq profiling (*14*) (**Fig. S3A**): they predominantly located within introns (n=648,244; 48.3%) and intergenic regions (n=404,499; 30.1%), and to a lesser extent at TSS-promoter regions (n=34,487; 2.57%). These regions occupy 12.3% of the genome and intersect with 89.1% of the 339,815 CREs identified by the ENCODE consortium (*20*) (**Fig. S3B**). Using this universal peak set, cells of the same lineage clustered together across tissues, such as immune cells (*e.g.,* T/NK cells, B cells, plasma cells, macrophages) and stromal cells (*e.g.,* adipocytes, pericytes), further validating the accuracy of cell annotations (**Fig. S3C**).

Using an entropy-based method(*12*), we identified 320,304 cis-regulatory elements (CREs) that are cell-type-specific (**Fig. S3D, Table S3; Methods**). We next applied chromVar (*21*) to pinpoint TF motifs specific to each cell type (**Fig. S3E**). The results were consistent with established findings, highlighting the enrichment of *Runx3* in cytotoxic T cells and NK cells (*22*), *Sfpi1* in general myeloid cells (*23*), *Irf4* in plasma cells (*24*), and *Ebf1* in B cells and pericytes (*25*, *26*) (**Fig. S3E**). The enrichment of these motifs was further validated by gene activity and cross-validated across different organs (**Fig. S3F**). Interestingly, we also observed TFs with a negative correlation between motif accessibility and gene activity, such as *Gfi1b* in erythroid cells (**Fig. S3F**), consistent with its role as a transcription repressor during erythroid development in humans(*11*, *27*).

Next, we sought to use cell-type-specific accessible peaks to interpret genetic variants associated with complex traits and diseases. Specifically, we first mapped human SNPs to orthologous coordinates in the mouse genome and then applied linkage disequilibrium score regression (LDSC) to assess GWAS SNP enrichment within cell-type-specific accessible peaks, similar to previous studies(*28*) (**Methods**). Given that many GWAS SNPs reside in non-coding regions, this analysis provides insights into their functional relevance by prioritizing cell types of interest (**Fig. S3G**). For instance, Alzheimer's disease SNPs were significantly enriched in microglia-specific CREs, consistent with prior studies(*29*). Meanwhile, SNPs associated with multiple sclerosis were enriched in B cells, T cells, and plasma cells(*30*, *31*), while LDL-associated SNPs were linked to hepatocytes(*32*) and height-associated SNPs were linked to tenocytes. SNPs for type II diabetes showed the strongest association with pancreatic beta cells(*33*), and those for hypertension with juxtaglomerular cells in the kidney(*34*) (**Fig. S3G**).

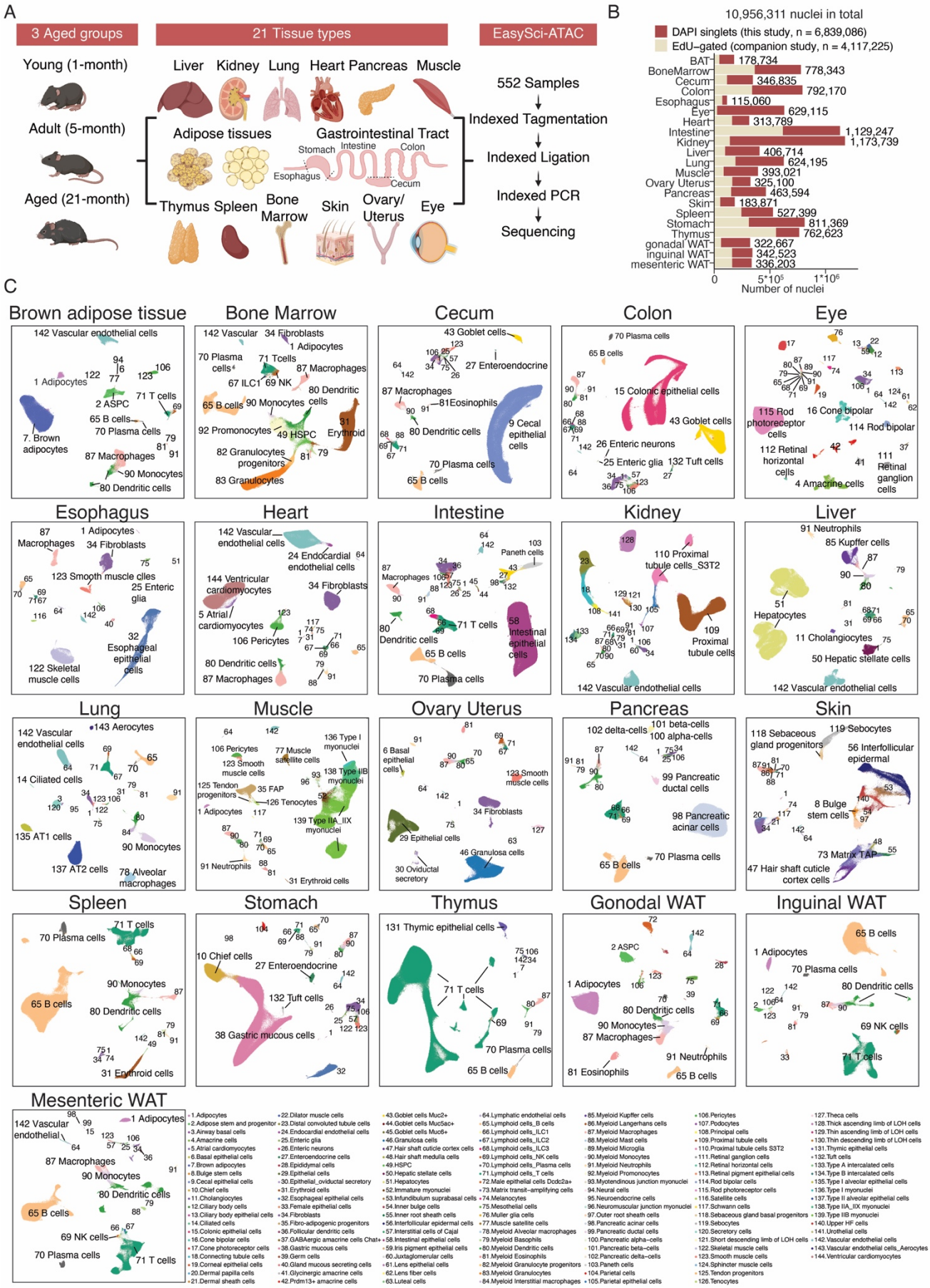

Figure 1. An organismal, single-cell chromatin accessibility atlas of aging.

(A) Experimental scheme to construct an organismal cell atlas of chromatin accessibility across different ages and both sexes.
(B) Barplot showing the number of cells profiled in each tissue, colored by the sources. DAPI singlets represent the global cell population investigated in this study.
(C) UMAP visualization of cells from each tissue, colored by 144 unique cell types collapsed from all tissues.

Age- and sex- dependent cell population change at the main cluster level

By quantifying cell type abundances in tissues from 5-month-old mice, we observed significant variability across organs, with both highly abundant populations (*e.g.,* hepatocytes, cecal epithelial cells, brown adipocytes) and rare, organ-specific cell types detected (**Fig. 2A**). Notably, 43 organ-specific cell types constituted less than 1% of their tissue's cellular composition, such as *Ascl1*+ neuroendocrine cells in the lung (0.039%) and *Gja8*+ lens epithelial cells in the eye (0.051%), underscoring the high sensitivity of scATAC-seq to identify low abundant but critical cell populations.

We next examined sex dimorphism for each main cell type. While most cell types exhibited similar population sizes between sexes (Pearson correlation r = 0.99, 0.98, 0.95 for young, adult and aged mice, respectively) (**Fig. S4A**), we identified a subset of cell types displaying strong sex-specific differences in chromatin states. Specifically, we trained k-nearest neighbor (KNN) classifiers to distinguish female and male cells of the same age for each cell type based on chromatin embeddings (**Methods**). We then used the area under the curve (AUC) metric to quantify classification accuracy, and cell types with AUC > 0.9 were considered to exhibit high sex-associated disparity (**Fig. 2B**). This approach revealed high sex-associated chromatin states in hepatocytes, proximal tubule cells, type IIB myonuclei, and multiple cell types from the gonadal white adipose tissue (*e.g.,* adipocytes, adipose stem and progenitor cells, mesothelial cells, and smooth muscle cells)(**Fig. 2B**), mirroring previous reports based on gene expressions (*7*, *35*, *36*). For example, proximal tubule (PT) cells in the kidney, including the general states spanning spatially connected segments (PTS1, PTS2 and PTS3; marked by *Slc34a1*) and a distinct state of segment 3 (PTS3T2, marked by *Slc22a7*) (*37*) was separated into clusters determined by sexes with unique marker gene accessibility (**Fig. 2C and Fig. S4B**). Furthermore, extensive changes underlying the sex difference were found on autosomal chromosomes and exhibited high cell-type-specificity (**Fig. 2C, right**).

We further investigated how aging influences the cell population dynamics across various tissues. Using linear regression, which included an age-sex interaction term, we pinpointed specific cell types that undergo significant changes with age within each organ (**Methods**). This analysis revealed that 146 organ-specific cell types are significantly altered upon aging (FDR of 0.05, $R^2 > 0.4$), with 55 of these showing significant differences between males and females in aging (**Fig. 2D-E; Table S4**). Although aging-associated changes were noted in all profiled tissues, certain organs (*e.g.,* ovary/uterus, liver, thymus) exhibited a higher proportion of cell types with significant age-related changes (**Fig. S5A**), suggesting higher susceptibility to the aging effects in these organs.

A total of 62 main cell types were significantly expanded in aging regardless of sex (**Fig. 2E, Fig. S5B top**). Notably, the majority (68%) of these aging-expanded cell types are immune cells distributed across various organs (**Fig. S5C**). Plasma cells and macrophages were among the most significantly expanded, showing an increased relative proportion in 14 and 12 tissues, respectively, indicating a widespread increase across the organism (**Fig. 2E**). Several less characterized cell population changes were detected across multiple organs, such as the expansion of dendritic cells in the BAT and stomach, and ILC3s in the liver, colon, and cecum (**Fig. S5D**). Additionally, we observed the expansion of other immune cell types with more tissue-specific distributions, such as Kupffer cells in the liver and gamma-delta (γδ) T cells in the iWAT (**Fig. S5D**), consistent with previous studies(*38–42*). In addition to immune cells, we detected a notable expansion of various non-immune cell types during aging. For example, specialized myonuclei associated with neuromuscular junctions (NMJs) and myotendinous junctions showed increased abundance (**Fig. 2E and 2F left**), potentially acting as a compensatory mechanism to maintain muscle integrity and contractile function under age-related stress(*43*). Furthermore, we observed a rise in enteroendocrine cells within the

stomach (**Fig. 2E and 2F left)**, which could contribute to dysregulated digestive processes in aged individuals (*44*). Notably, these expansions were consistent across different sexes and were further validated by re-analysis of an independent single-cell transcriptome atlas of aging(*7*) (**Fig. 2F, right).**

The 29 aging-depleted cell types are predominantly tissue-specific (**Fig. 2E, Fig. S5B bottom**). This includes a notable reduction in immune cell progenitors such as pro-/pre-B cells in the bone marrow, which contributes to the age-related decline in immune function (*45*). Similarly, in the thymus, there is a decrease in immature T cells during the double-negative (DN) and double-positive (DP3) stages, indicative of diminished T cell production in the aging thymus (*46*). Other aging-depleted immune cell types, like NK cells and pDC cells in the spleen, were also detected, aligning with previous findings (*47*, *48*) (**Fig. 2E, Fig. S5B, S5E**). Meanwhile, multiple non-immune cell types are significantly depleted across organs, especially in the ovary/uterus, skin, and lung (**Fig. S6A**). In the ovary/uterus, for example, granulosa cells and theca cells that collaborate in sex hormones production decline with age, together with basal epithelial cells and vascular endothelial cells. (**Fig. 2E, Fig. S6B**). This aligns with the decrease in ovarian follicles that characterizes reproductive aging (*49*, *50*). In the skin, aging is associated with fewer melanocytes—a trend consistent with a 10–20% reduction per decade in individuals over 25–30 years of age (*51*)—as well as lower proportions of dermal papilla cells, outer root sheath cells, and lymphatic endothelial cells (**Fig. 2E, Fig. S6B**), the latter consistent with reduced skin lymphatic density observed in aging(*52*). Similarly, the aged lung exhibits declines in stromal cell types associated with blood vessels, including pericytes, smooth muscle cells (**Fig. 2E, Fig. S6B**), and a specialized endothelial cell type known as aerocytes(*53*) (**Fig. 2F**). These cells are important for maintaining proper vascular structure and function, suggesting that their depletion may contribute to compromised blood flow regulation in the elderly lung(*54*).

Moreover, we observed a decline in other functional cell types, such as kidney podocytes that filter primary urine from plasma (**Fig. 2E-F)**, aligning with previous studies(*55*). The depleted cell populations also include a group of less characterized *Ncam1*+ parietal epithelial cells (**Fig. 2E, Fig. S6B)**, which serve as progenitor cells capable of proliferation and differentiation into podocytes (*56*). The depletion of both mature podocytes and their precursor cells could contribute to the impaired capacity of the kidney to regenerate and maintain proper filtration over time. Additionally, aging-depleted cell types include liver hepatocytes (*57*), muscle tenocytes(*58*), muscle satellite cells (*59*), stomach enteric neurons, and adipocytes from multiple organs (*e.g.,* lung, gWAT, and ovary/uterus) (**Fig. 2E-F and S5B),** validated by re-analysis of external single-cell transcriptome dataset(*7*) (**Fig. 2F)**. Interestingly, some of these aging-decreased cell types (*e.g.,* muscle satellite cells and tenocytes, bone marrow pro-/pre-B cells) exhibited reductions of more than 50% at relatively early stages (between 1 and 5 months) (**Fig. 2F, S5B bottom, S6B**), highlighting an early onset of aging impacts on the population of these cell types.

We further analyzed 55 cell types displaying significant age-sex interactions. Most sex-specific cell types (35 out of 55) are immune cells, including 19 that preferentially expanded in aging females and 15 in aging males (**Fig. 2G)**. For instance, aged male mice showed significant increases in neutrophils (in the lung and intestine) and eosinophils in the muscle (**Fig. 2G)**, consistent with male-specific expansions of these cells observed in prior human studies(*60*, *61*). Conversely, aged females demonstrated increased populations of basophils (in the liver) and NK cells (in the pancreas and bone marrow) (**Fig. 2G)**. Additionally, some cell types exhibited similar trends in both sexes but differed in the extent of change in different organs. For example, ILC2 cells in the bone marrow and hepatic stellate cells in the liver expanded more significantly in males, whereas the increase of interstitial macrophages in the lung and depletion of naive/memory B cells in the spleen was more pronounced in the female (**Fig. 2G-H)**. Interestingly, certain cell types showed opposite trends between the sexes. For instance, the aforementioned specialized proximal tubule (PT) cell

type (PT S3T2, characterized by *Slc22a7*) increased in females but decreased in males, whereas the other PT cells (PT S1S2S3, marked by *Slc34a1*) exhibited the opposite pattern (**Fig. 2I)**. The findings were further validated by re-analysis of independent single-cell transcriptome atlas profiling both adult and aged tissues (*7*) (**Fig. 2J).**

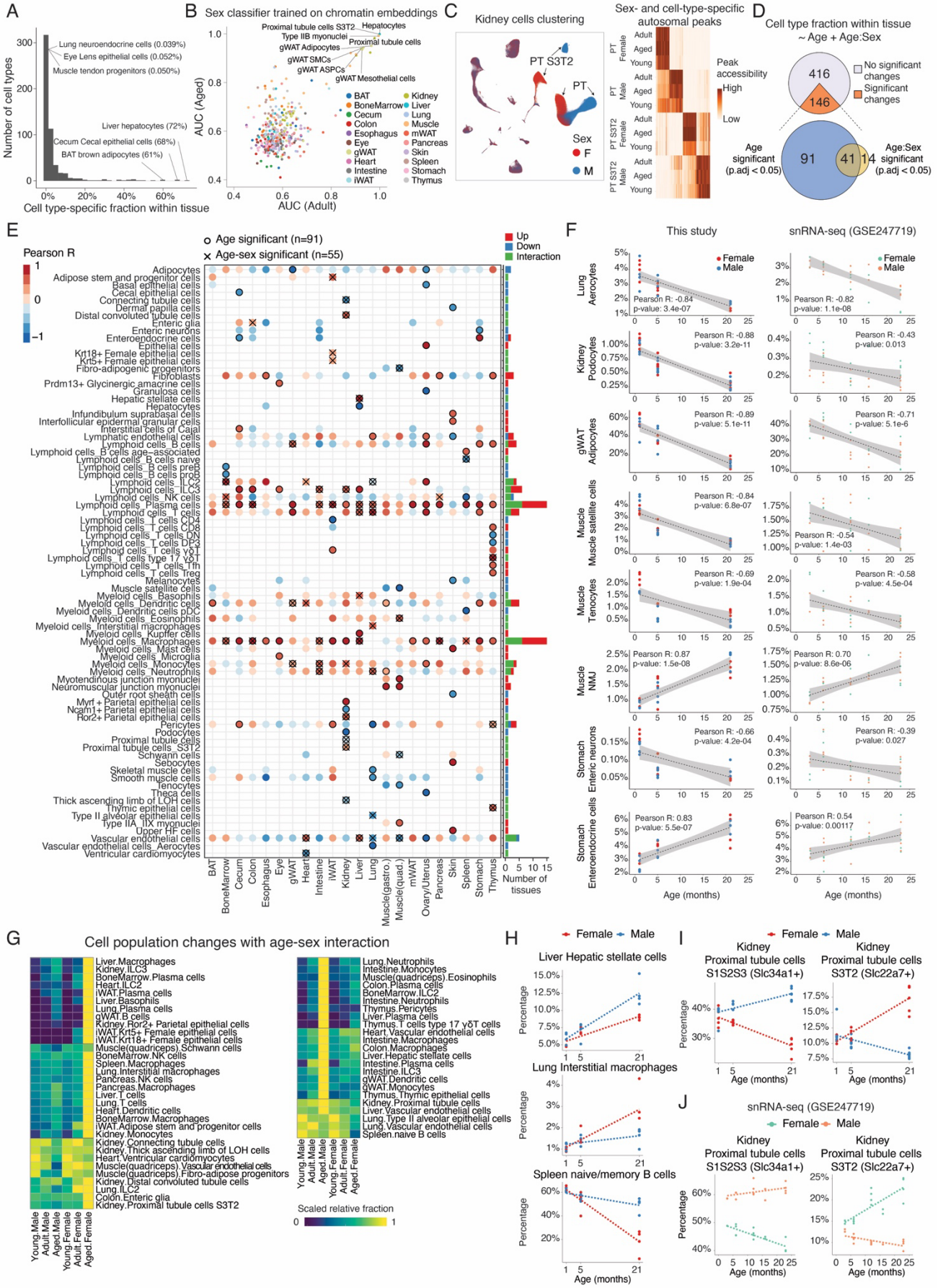

Figure 2. Age- and sex-dependent cell population changes at the main cell type level.
(A) Histogram showing the distribution of cell type specific fractions within tissue. Only cells from adult mice (5-month-old) were used in this quantification.
(B) K-means classifiers were trained to distinguish male and female cells for each main cell type using spectral embedding calculated by SnapATAC2 (*17*). Scatterplot comparing the area under the curve (AUC) values of models between adult and aged cells. Cell types with high sex dimorphism in both age groups are labeled.
(C) Left: UMAP plots of all kidney cells, colored by sex (right), highlighting distinct chromatin states between sexes of proximal tubule cells (PT). Right: Heatmap displaying accessibility of autosomal peaks with sex- and cell-type-specific patterns, conserved across ages.
(D) Venn diagram showing the number of main cell types whose relative proportions in corresponding tissues are significantly associated with age or age-sex interactions.
(E) Left: Dotplot showing all significantly altered main cell types from (D) across tissues, colored by Pearson correlation between their relative proportion and age. Cell types with significant age or age-sex interactions are marked. Right: Barplot summarizing the number of tissues with significant changes for each cell type, colored by direction (up/down) or interaction.
(F) Scatterplot illustrating examples of main cell types with significant age-related proportional changes (left), alongside validation using published snRNA-seq data (*7*) for the same cell type and tissue (right).
(G) Heatmap showing relative proportions of main cell types with significant age-sex interactions, including female-biased (left) and male-biased (right) cell types.
(H) Scatterplot highlighting cell types that change in the same direction with aging but exhibit sex-dependent magnitude.
(I-J) Scatterplots of two kidney proximal tubule cell types with opposite sex-specific proportional trends **(I)** and snRNA-seq validation results **(J).**

Age- and sex- dependent cell population change at the subtype level

We further explored cell population dynamics at the subtype level. First, we re-clustered each main cell type using *SnapATAC2(17)*, and manually curated cellular subtypes based on cluster-specific gene accessibility. Our analysis revealed significant heterogeneity within main cell types. For instance, amacrine cells in the eye, known for their extensive diversity(*62*), were clustered into thirty-four distinct subtypes (**Fig. 3A**). These subtypes were characterized by unique gene activity, peak accessibility, and TF motif enrichments (**Fig. 3A, Fig. S7A-B**), aligning with previous findings based on single-cell transcriptomic analyses (*62*). In total, our clustering analysis identified 1,828 subtypes from 386 main cell types across the entire organism, with a median of 1,610 cells per subtype and four subtypes per main cell type (**Fig. S7C**). Most subtypes (93.4%) were consistently detected across more than ten samples (**Fig. S7C**). Notably, we identified many rare cell subtypes that have not been extensively explored in prior chromatin accessibility studies. Notable examples include diverse enteroendocrine cells in the small intestine, including L cells (marked by *Gcg*, 0.092% of the total population), K cells (marked by *Gip*, 0.070%), D cells (marked by *Sst*, 0.028%), enterochromaffin cells (marked by *Tph1*, 0.084%), and enteroendocrine progenitor cells (marked by *Neurog3*, 0.081%) (**Fig. S7D-S7E**).

We next investigated cell population changes at the subtype level. Using the same analytical pipeline for identifying aging-associated main cell types, we identified 499 subtypes (out of 228 organ-specific main cell types) with significant cell population dynamics associated with aging (FDR of 0.05, $R^2 > 0.4$) (**Fig. 3B, Table S5**). Of these, 193 subtypes exhibited significant sex-specific aging differences (FDR of 0.05) (**Fig. 3C**). A median of 24 significantly altered subtypes was identified per tissue, ranging from 51 in the kidney to 3 in the esophagus (**Fig. 3C**). While the dynamics of aging-associated subtypes were generally consistent with their main cell type changes (Pearson r: 0.72, p-value < $2.2 * 10^{-26}$), distinct trends emerged in certain subtypes compared to their parent main cell types (**Fig. 3D**). For instance, specific aging-associated subtypes such as *Lepr1*+ *Abcg1*+ fibroblasts and *Ccr3*+ *C5ar1*+ *C5ar2*+ mast cells expanded in the aged intestine, while their main cell types remained relatively stable with age (**Fig. S7F-G**). In the liver and lung, while the overall main T cell population increased in aged tissues, subtypes corresponding to naive T cells were depleted (**Fig. S7F-G**). In contrast, we observed an expansion of a subtype corresponding to *Il10*+ *Foxp3*+ regulatory T cell in the iWAT, despite the overall CD4 T cell proportion decreasing with aging (**Fig. S7F-G**). We also observed opposing aging-associated dynamics of subtypes from the same cell type. For example, in the bone marrow hematopoietic stem and progenitor cells (HSPCs), there is a marked decrease in lymphoid progenitors (HSPC-3, marked by *Il7r (63)*), accompanied by a significant expansion of aging-associated megakaryocyte progenitors (HSPC-4, marked by *Gata2, Fhl1, and Hoxb5*) (**Fig. 3E-F)**, consistent with findings from a recent study(*64*).

Several aging-associated subtypes correspond to the same cell type in distinct spatial locations, uncovering region-specific vulnerabilities during aging. For example, renal vascular endothelial cells (ECs) can be clustered into heterogeneous subtypes representing ECs from different anatomical locations within the nephron(*65*), including the artery (*Sox6*+), cortex (*Npr3*+*, Igfbp3*+), vein (*Lhx6*+), medulla (*Igf1*+*, Cyp1b1*+), vasa recta (*Aqp1*+), and glomeruli (*Gata5*+) (**Fig. 3G-H**). Interestingly, while the total abundance of ECs remains relatively unchanged at the main cell type level, we observed a pronounced depletion of two EC subtypes—*Lhx6*+ vein ECs and *Igf1*+*, Cyp1b1*+ medulla ECs (**Fig. 3I**)—indicating that endothelial cells in these specific regions are more vulnerable to aging. The findings were further validated through a published snRNA-seq dataset(*7*): we observed a consistent decline of *Igf1*+ *Cyp1b1*+ medulla ECs across aging in both sexes, despite a higher baseline proportion in females (**Fig. 3J-K)**.

Meanwhile, certain aging-associated cell subtypes across different spatial locations share similar molecular features. For example, sub-clustering analysis of three specialized renal epithelial cell types—the thick ascending limb of the Loop of Henle (TAL), distal convoluted tubule (DCT), and connecting tubule (CNT)—revealed three subtypes (*i.e.,* TAL-5, DCT-4, and CNT-5) that exhibit significant expansion in aging (**Fig. 3L-M)**, particularly in females. All three subtypes converged into a reactive aging-associated epithelial cell state that is characterized by the activation of transcription factors linked to inflammation and stress responses (*e.g., Creb5, Bnc2, Runx1, Bach2, Fosl2,* and *Klf7***)**, confirmed through gene body accessibility (**Fig. 3N**) and TF motif activity (**Fig. 3O)**. We further validated the existence of these states (**Fig. 3P**) and female-biased expansions (**Fig. 3Q**) by re-clustering the same cell type from a single-cell transcriptomic atlas of aging(*7*). The emergence of this reactive cellular state underscores the potential influence of inflammatory signaling on epithelial cells specifically in the aged female kidney. In summary, our subtype-level analysis revealed both region-specific and shared aging-associated changes.

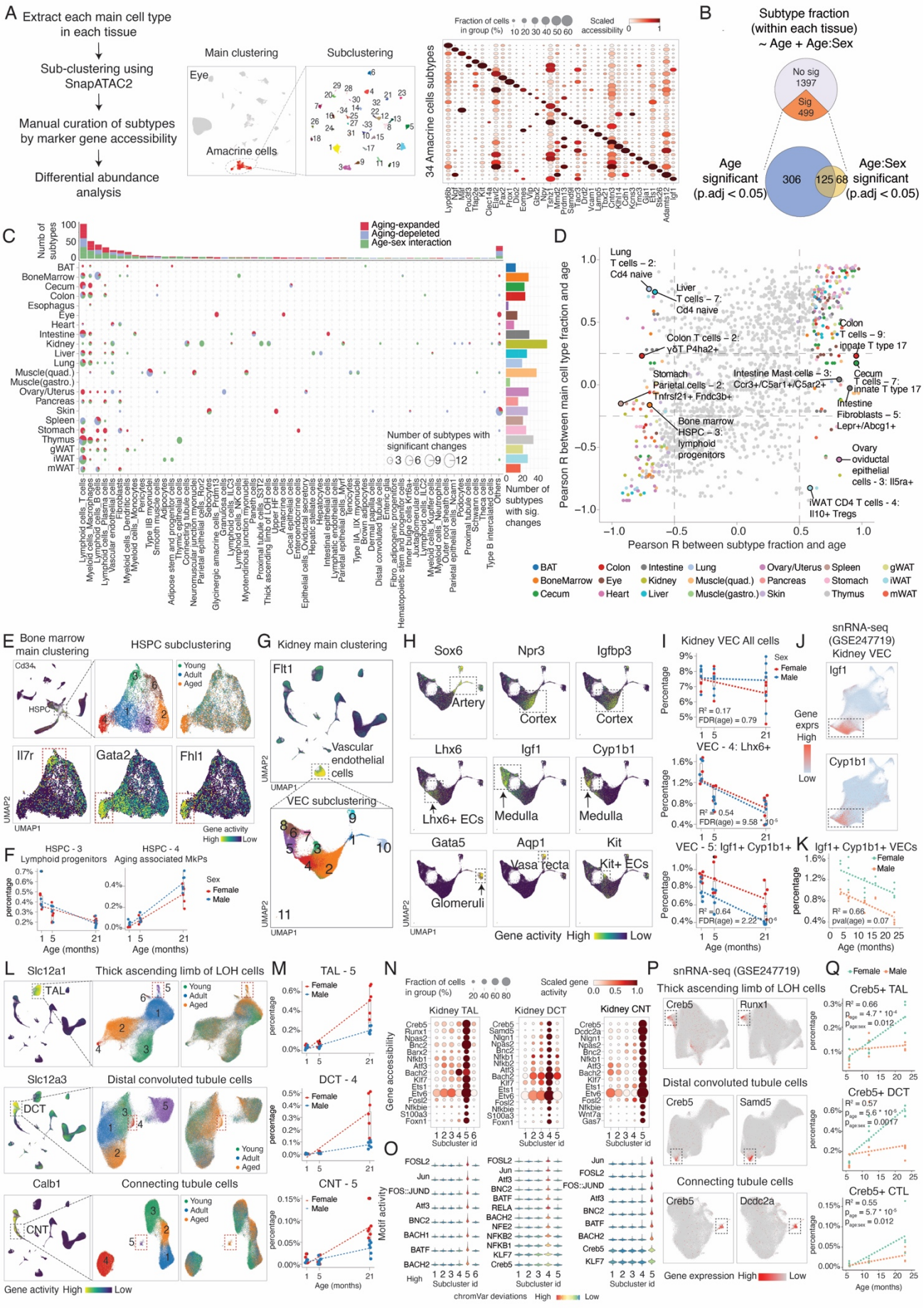

Figure 3 Age- and sex-dependent cell population change at the subtype level.

(A) Left: schematic of the sub-clustering workflow. Middle: example UMAP plots showing sub-clustering analysis of eye amacrine cells, colored by subcluster ID. Right: dotplot displaying marker gene accessibility for amacrine cell subtypes.

(B) Venn diagram showing the number of cell subtypes with significant changes associated with age or age-sex interactions.

(C) Top: barplot showing the number of aging-associated subtypes for each main cell type. Center: dotplot summarizing the number aging-associated subtypes across main cell types and tissues. Right: barplot showing the number of aging-associated subtypes per tissue.

(D) Scatterplot comparing aging-associated cellular fraction changes between aging-associated subtypes and their corresponding main cell types. Subtypes with distinct trends compared to their parent main cell types are labeled.

(E) UMAP plots showing sub-clustering of bone marrow HSPCs to identify different subtypes, colored by subcluster ID (top middle), age group (top right), and marker gene accessibilities for lymphoid progenitor cells (bottom left) and age-associated megakaryocyte progenitors (bottom right).

(F) Scatter plot showing cell proportion changes for lymphoid progenitor cells (HSPC-3) and age-associated megakaryocyte progenitors (HSPC-4), with a linear regression fit. Each dot represents one animal.

(G) UMAP plot showing sub-clustering results of kidney vascular endothelial cells to identify different subtypes, colored by subcluster ID (bottom).

(H) UMAP plots of kidney vascular endothelial cells, colored by the accessibility of genes that mark vascular cells across different spatial locations.

(I) Scatter plots and boxplots showing the fractions of all kidney endothelial cells (top), vein endothelial cells (*Lhx6*+ VEC-4, center), and medulla endothelial cells (*Igf1*+ *Cyp1b1*+ VEC-5, bottom) across three age groups.

(J) UMAP plots of vascular endothelial cells from a published snRNA-seq study (*7*), colored by the expression of genes marking medulla endothelial cells (as in **H**).

(K) Scatterplot showing the aging-associated decline in the kidney medulla endothelial cells identified from a snRNA-seq atlas of aging(*7*).

(L) UMAP plots showing all kidney cells (Left) and sub-clustering analysis (middle and right) for thick ascending limb cells (TAL, top), distal convoluted tubule cells (DCT, center), and connecting tubule cells (CNT, bottom), colored by main cell type specific markers (left), subtype ID (middle) and age group (right). Squares indicate the aging-associated cell subtypes.

(M) Scatter plots showing the relative fractions of three reactive subtypes identified in (**K**) across ages, with separate linear regression fits for each sex.

(N) Dotplots showing the gene marker accessibility marking the reactive states (TAL-5, DCT-4 and CNT-5) in each renal epithelial cell type.

(O) Violinplots showing the motif accessibilities of transcription factors marking the reactive states in each renal epithelial cell type.

(P) UMAP plots showing sub-clustering results for TAL, DCT, and CNT cells from published snRNA-seq data(*7*), colored by the expression of genes that mark reactive states (as in **N**).

(Q) Scatterplots showing the relative fractions of reactive subtypes identified in **(P)** across aging, with separate linear regression fits for each sex.

Aging-associated population dynamics of broadly distributed immune subtypes

We next examined whether broadly distributed cells displayed similar dynamics across multiple organs in aging. We first analyzed immune cells, including T cells (n = 1,264,322 cells), B cells (n = 1,079,641 cells), plasma cells (n = 157,545 cells), innate lymphoid cells (NK cells, ILC1, ILC2 and ILC3) (n = 87,550 cells), monocytes and macrophages (n = 581,877 cells), and dendritic cells (n = 306,562 cells) isolated from various organs.

Clustering analysis for each cell type revealed a total of sixty-seven highly heterogeneous immune cell subtypes, each defined by distinct chromatin accessibility patterns at key marker genes (**Fig. 4A-B**). For instance, the combined clustering of T cells yielded sixteen subtypes spanning a differentiation trajectory from T progenitor/double-negative (DN) cells, through double-positive (DP) cells, and onward to mature T cell states (**Fig. 4A-B, top left**), including CD4 T cells (*Cd4*+), CD8 T cells (*Cd8b1*+), γδ T cells (*Tcrg-C4*+), and innate-like T cells (*Zbtb16*+) (**Fig. S8A**). Similarly, we identified eight B cell clusters forming a trajectory from pro-B and pre-B cells (*Erg*+*, Rag1*+*, Il7r*+) through naive/memory B cells (*Cd55*+*, Fcer2a*+) and finally transitioned into aging-associated states marked by either *Tbx21* or *Pstpip2* (**Fig. 4A-B, top right; Fig. S8B**). These aging-associated B cell states closely mirror recent single-cell transcriptomic findings(*66*). Within the plasma cell population, we detected IgA, IgM, and IgG plasma cells, each comprising several distinct subtypes (**Fig. 4A-B, middle left**). For innate lymphoid cells, ten clusters were identified, including multiple subtypes within NK cells, ILC2, and ILC3 (**Fig. 4A-B, middle right; Fig. S8C**). Monocytes and macrophages were resolved into twelve subtypes (**Fig. 4A-B, bottom left**), capturing the transition from *Ace*+ monocytes to *Lyve1*+ tissue-resident macrophages, and various specialized macrophages across different tissues. Dendritic cells (DC) were categorized into fourteen subtypes (**Fig. 4A-B, bottom right**), including *Xcr1*+ type I DCs, *Sirpa*+ type II DCs, *Ccr7*+ migratory DCs, and *Siglech*+ plasmacytoid DCs, with diverse subsets observed within each major type.

We then quantified the tissue composition of each immune subtype. Although many subtypes were detected globally, certain subtypes exhibited high organ specificity (**Fig. 4C**). For example, immature T cells (T cells -1, T cells - 2, T cells -3, and T cells - 4) were predominantly in the thymus, while *Gzma*+ γδ T cells (T cells - 13) were mainly localized to the intestine, cecum, and colon(**Fig. 4C**). Similarly, B cell progenitors (B cells - 1 and B cells - 2) were primarily found in the bone marrow, and IgA+ plasma cells (plasma cells - 1, plasma cells -2, and plasma cells - 3) were enriched in gastrointestinal organs (*e.g.,* intestine, cecum, and colon)(**Fig. 4C**). For macrophages (MAC), *Cxcl16*+ *Tlr12*+ macrophages (MAC-6 and MAC-7) were constrained to the small and large intestine, while *Spic*+ macrophages were unique to bone marrow (MAC-9) and spleen (MAC-10)(**Fig. 4C**). The latter aligns with previous reports about the role of *Spic* in the development of iron-recycling macrophages in these two organs(*67*). Certain dendritic cells also demonstrated tissue-specific characteristics, such as *Apol7c*+ type I DCs (DC-3), *Il22ra2*+, and *C1qtnf3*+ type II DCs (DC-9 and DC-10), which were exclusively identified in the gut(**Fig. 4C**).

We next assessed how these immune subtypes changed with aging (**Fig. 4D**). Six immune subtypes were found significantly depleted across multiple tissues, including naive CD4+ T cells in ten tissues, naive CD8+ T cells in five tissues, and immature B cells in the bone marrow, spleen, and mWAT(**Fig. 4D**). We also observed a significant depletion of organ-specific immune progenitor cells, such as immature T cells in the thymus and pro-B/pre-B cells in the bone marrow, which subsequently led to a reduction of naive/memory B cells in tissues like the spleen and mWAT(**Fig. 4D**). In addition, we uncovered less-characterized immune cell dynamics validated across multiple organs. For instance, *Zfp683*+ tissue-resident memory T cells were consistently depleted in the intestine, iWAT, and mWAT (T cells - 12, **Fig. 4D**), and *Gzma*+ resting NK cells (*68*) were depleted in both the spleen and bone marrow (NK - 1; **Fig.**

4D). Notably, the depletion of this resting NK cell subtype occurred concurrently with an expansion of a *Gpr55*+ *Ifi211*+ proinflammatory NK cell subtype (*69*) (NK - 3) in the same organs (**Fig. 4D**).

In contrast to these depletions, the majority of immune subtypes (42 out of 67) significantly expanded during aging in at least one tissue (**Fig. 4D**). These expansions included nine T cell subtypes, eight NK and ILC subtypes, five B cell subtypes, seven dendritic cell subtypes, and nearly all plasma cell and monocytes/macrophages ('MoMa') subtypes (**Fig. 4D**). Notable examples of broadly expanding populations included *Zbtb16*+ *Il23r*+ type 17 innate T cells (T cells - 15), *Gzmk*+ CD8 T cells (T cells - 10), *Il21*+ follicular helper T cells (T cells - 9), *Foxp3*+ regulatory T cells (T cells - 7), *Tbx21*+ aging-associated B cells (B cells - 6), *Chst1*+ *Wipf3*+ IgM plasma cells (plasma cells - 5), *Clec4d*+ monocytes (MoMa - 4), and *F13a1*+ *Lyve1*+ macrophages (MoMa - 5), each of which expanded in multiple organs (**Fig. 4D**). Beyond these widespread patterns, some aging-associated expansions were confined to specific organs. For example, several immune subtypes expanded preferentially in the gastrointestinal tract, such as *Gpr15*+ *Stc2*+ IgA plasma cells (plasma cells - 3; **Fig. 4E-F, left**), *Tlr12*+ macrophages (macrophages - 7; **Fig. 4E-F, right**), *Ccr6*+ *Trappc3l*+ ILC3 cells (NK/ILC - 7), and *Apol7c*+ type I DCs (dendritic cells - 3) (**Fig. 4D**). We also identified tissue-specific expansions of *Cd163l*+ *Sox13*+ ILC3 cells (NK/ILC - 8) in the eye, kidney, and liver, as well as *Pcsk1*+ ILC2s (NK/ILC - 9) in the ovary/uterus and *Cybb*+ ILC2s (NK/ILC - 10) in the bone marrow (**Fig. 4D**). Interestingly, some immune subtypes exhibited opposite trends depending on the organ. For instance, *Klrk1*+ *Gas7*+ CD8 effector T cells (T cells - 8) expanded in the liver and lung but were depleted in gastrointestinal tissues (*e.g.,* colon and cecum) (**Fig. 4D**), potentially due to distinct local microenvironmental cues that shape tissue-specific aging dynamics.

Aging-associated immune cell dynamics also differed notably between males and females. For example, *Gzmk*+ CD8 exhausted T cells exhibited greater expansion in females (**Fig. 4G, left**), notably in the lung, pancreas, and mWAT, while type 17 innate T cells showed a stronger increase in males, especially in the stomach, gWAT, and mWAT (**Fig. 4G, right)**. Overall, however, we observed that females tend to have a greater expansion of immune cell subtypes than males during aging (53 female-biased subtypes compared to 31 male-biased subtypes, **Fig. S8D**), including *Tbx21*+ aging-associated B cells (in mWAT, pancreas, thymus; **Fig. 4H**), *Gpr55*+ *Ifi211*+ NK cells (in bone marrow, pancreas, iWAT, spleen; **Fig. 4I-J, left**), *Sox5*+ *Ifnlr1*+ *Zfp362*+ macrophages (in thymus, gWAT; **Fig. 4I-J, middle**) and *Dtx1*+ *Sripb1a*+ type II dendritic cells (**Fig. 4I-J, right**). These subtypes potentially contribute to the higher prevalence of autoimmune diseases in women(*70*). Interestingly, we observed an enrichment of male-biased subtypes within gastrointestinal tissues, with 15 out of 31 originating from the esophagus, stomach, intestine, cecum, and colon, compared to only 2 out of 53 in female-biased ones (**Fig. S8D**). Noteworthy examples include the expansion of *Ccr9*+ ILC3s (NK/ILC-5) and *Cyp26b1*+ ILC3s (NK/ILC-6) in the intestine (**Fig. S8D**), reflecting more pronounced changes in the innate immunity during male intestinal aging (*71*).

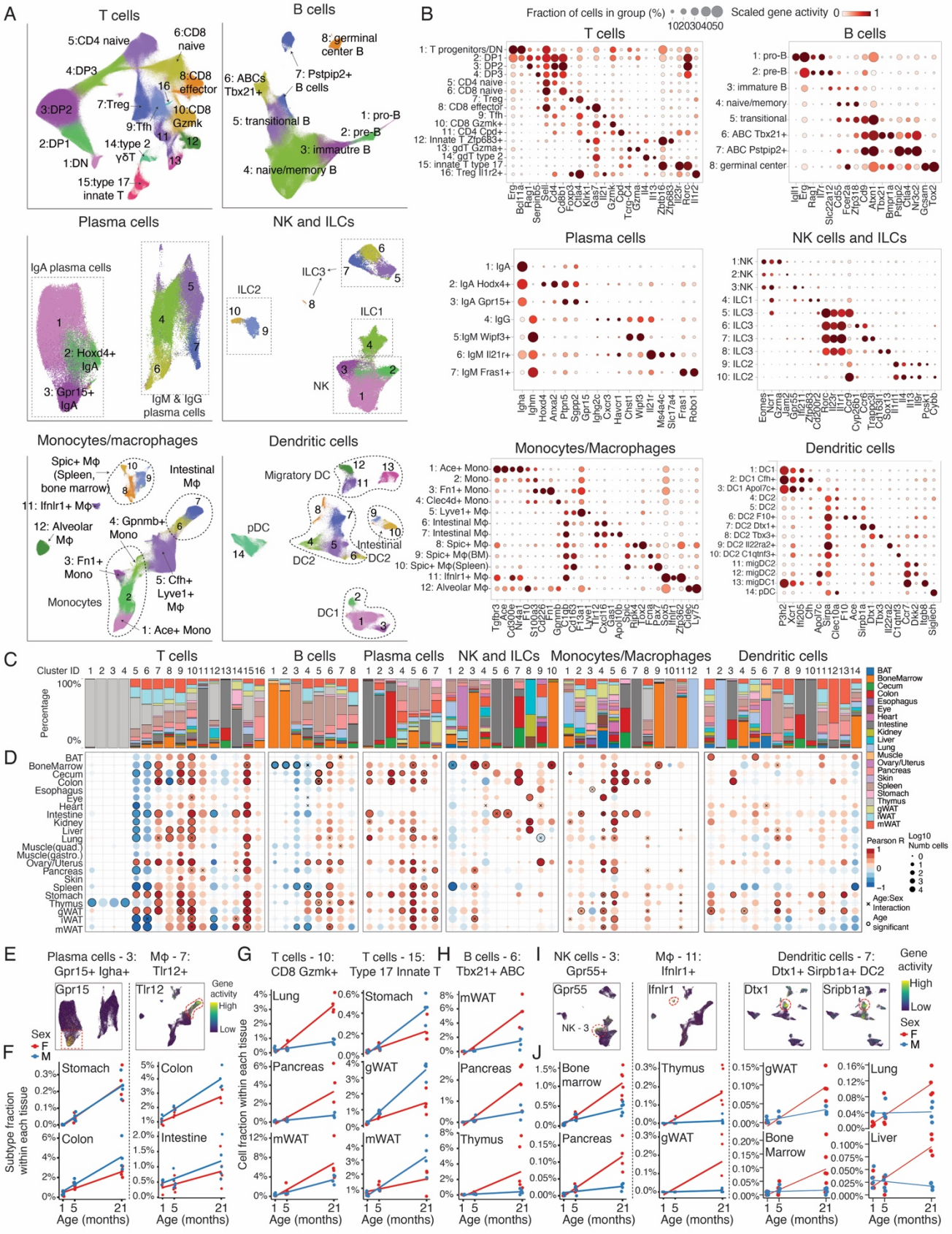

Figure 4. Aging-associated dynamics of broadly distributed immune subtypes.

(A) UMAP plots showing combined clustering results for T cells, B cells, plasma cells, innate lymphoid cells, macrophages and dendritic cells across tissues, colored by subtype id.

(B) Dotplots showing accessibilities of genes used for annotating immune cell subtypes.

(C) Stacked bar plots showing the tissue composition for each immune subtype.

(D) Dotplots showing the proportional changes of each immune subtype in each tissue across aging, colored by Pearson correlation between their relative proportion (within each tissue) and age. Subtypes with significant age or age-sex interactions are marked.

(E) UMAP plots highlighting aging-expanded subtypes of plasma cell (left) and macrophage (right) in gastrointestinal tissues, colored by marker gene accessibility (*Gpr15* for plasma cell-3 and *Tlr12* for macrophage-7).

(F) Scatterplot showing the relative fractions of *Gpr15*+ *Igha*+ plasma cells and *Tlr12*+ macrophages along aging.

(G) Scatterplots showing the relative fractions of *Gzmk*+ CD8 T cells (left) and *Il23r*+ *Zbtb16*+ type 17 innate T cells (right) along aging, with separate linear regression fits for each sex.

(H) Scatterplot showing the relative fractions of *Tbx21*+ aging-associated B cells along aging, with separate linear regression fits for each sex.

(I) UMAP plots showing subtypes exhibiting female-biased expansion along aging, colored by accessibilities of marker genes. (*Gpr55 for NK-3*, *Ifnlr1* for macrophage-11, *Dtx1* and *Sirbp1a* for dendritic cells-7).

(J) Scatterplot showing the relative fractions of *Gpr55*+ NK cells (left), *Ifnlr1*+ macrophages (middle) and *Dtx1*+ *Sirbp1a*+ type 2 dendritic cells (right) along aging, with separate linear regression fits for each sex.

Aging-associated population dynamics of broadly distributed non-immune subtypes

Next, we expanded our analysis to aging-associated dynamics in non-immune cell populations, focusing on vascular endothelial cells (VECs) (n = 426,160 cells, **Fig. 5A-B, top**), fibroblasts (n = 377,181 cells, **Fig. 5A-B, middle**), and smooth muscle cells (n = 101,284 cells, **Fig. 5A-B, bottom**), which are broadly distributed across organs. Unlike immune cells that share molecular states across tissues, these non-immune cell populations displayed remarkable organ specificity, with most (34 out of 61) clusters dominated by a single tissue (>90% of cells from one tissue). For example, we identified VECs specific to the liver (marked by *Gata4*) and the lung (marked by *Foxf1*) (**Fig. 5C**). The tissue specificity was further confirmed through motif footprinting analyses of marker TFs (**Fig. 5D**), and consistent with previous study (*72*). Similarly, tissue-specific TFs were observed in different fibroblast populations: *Six1* in bone marrow fibroblasts, *Foxf1* in gastrointestinal fibroblasts, *Tbx20* in cardiac fibroblasts, *Hoxc9* in kidney fibroblasts, and *Tbx5* in lung fibroblasts (**Fig. 5E**). We also identified subtypes exhibiting sex specificity. For instance, we identified subtypes of smooth muscle cells unique to female gonadal organs (*e.g.,* ovary, uterus, and gWAT). These cells were marked by the transcription factors *Wt1* and *Esr1,* supported by both gene accessibility and motif activity (**Fig. 5F**).

We further examined how these broadly distributed non-immune subtypes changed with aging (**Fig. 5G**). Compared to immune cells that overall expand across organs, these broadly distributed non-immune cell types exhibited strong tissue-specific changes during aging (**Fig. 5G**). For example, we observed an age-associated depletion of various organ-specific endothelial subtypes, such as cells in the kidney (VEC-14, *Igf1*+ kidney medulla endothelial), lung (VEC-7, *Tbx2*+ lung aerocytes), and muscle (VEC-1, *Aqp7*+) (**Fig. 5G and S9A**). By contrast, organ-specific endothelial cells in the liver (VEC-9, *Clec4g*+ sinusoidal endothelial) and pancreas (VEC-4, *Lamb1*+ VECs) expanded significantly during aging (**Fig. 5G and S9B**). The expansion of liver sinusoidal endothelial cells aligns with previous findings from *Tabula Muris Senis(57)*. Fibroblasts (FB) likewise displayed tissue-specific aging trajectories, showing expansion in aged bone marrow (*Btla*+ FB-13), colon (*Edil3*+ FB-21), cecum (*Prkcq*+ FB-19), stomach (*Csf2rb*+ FB-3), and mWAT (*Nkx6-1*+ FB-17) (**Fig. 5G and S9C**). In contrast, two fibroblast subtypes (ovary *Tgfa*+ FB-9 and stomach *Sox6*+ FB-23) significantly decreased in aging (**Fig. 5G and S9D**). For smooth muscle cell (SMC) subtypes, there is a strong depletion of several subtypes across organs, such as colon (*Hoxd3*+ SMC-15), lung (*Tbx5*+ SMC-3), and ovary/uterus (*Gata2*+ SMC-2) (**Fig. 5G and S9F**). In the cecum, however, there was an increased population of SMCs marked by inflammatory gene markers such as *Il7* and *Serpina1c* (SMC-5, **Fig. 5G and S9G**).

Importantly, we identified several cell subtypes that shared similar aging dynamics across multiple tissues. For example, a *Slc7a14*+ *Lhx6*+ *Meox2*+ vein endothelial cell subtype (VEC-5) was significantly depleted in several aged tissues (*e.g.,* muscle, gWAT, and ovary/uterus) (**Fig. 5H-II**), which could contribute to the endothelium dysfunction in aging. Likewise, an aging-associated fibroblast subtype characterized by elevated inflammatory markers (*e.g., Ifi207*, *Ifi205*, *Ear1*) expanded in several aged organs (*e.g.,* mWAT, stomach, cecum, esophagus) in a male-specific manner (**Fig. 5J-K**). Of note, these aging-associated subtype dynamics were validated through external datasets (*7*), such as the depletion of *Lhx6*+ endothelial cells in gWAT (**Fig. 5L-M)** and the expansion of *Csf2rb*+ fibroblasts in the stomach (**Fig. S9E**).

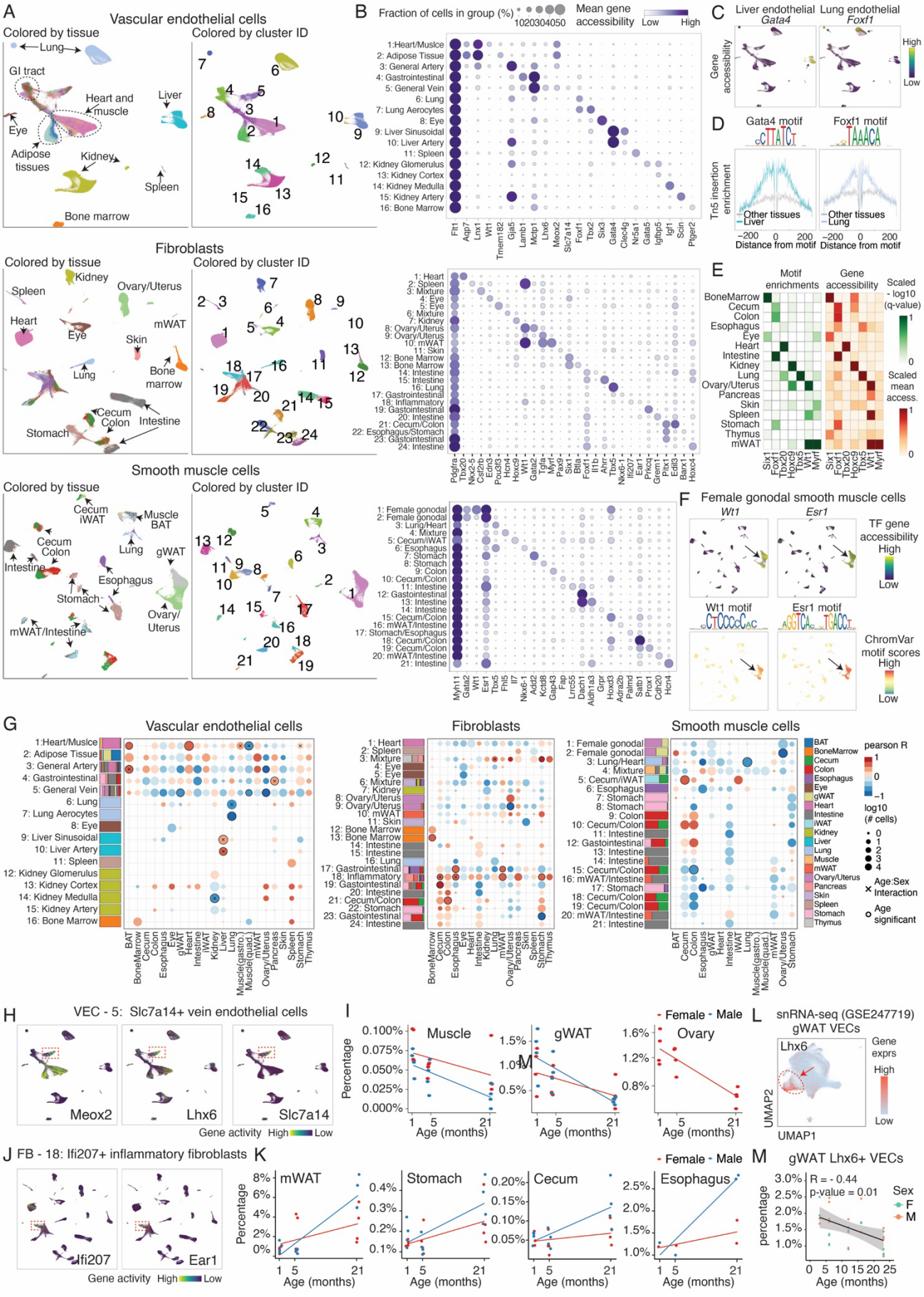

Figure 5. Aging-associated dynamics of vascular endothelial cells, fibroblasts, and smooth muscle cells across organs.

(A) UMAP visualization showing the combined clustering for vascular endothelial cells (VECs, top), fibroblasts (FBs, middle) and smooth muscle cells (SMCs, bottom) across tissues, colored by tissue origin (Left) and cluster ID (Right).

(B) Dot plots showing the accessibility of marker genes for cell clusters of VEC (top), FB (middle) and SMC (bottom), including a general marker for each cell type (*Flt1* for VEC, *Pdgfra* for FBs, *Myh11* for SMCs)

(C) UMAP plot of VECs colored by accessibilities of the liver VEC marker *Gata4* and lung VEC marker *Foxf1*

(D) Motif footprinting analysis showing enrichment of GATA4 motifs in liver VECs and FOXF1 motifs in lung VECs compared with other tissues.

(E) Heatmaps showing the motif enrichments and gene body accessibility of tissue-specific transcription factors. Motif enrichment scores (-log10 q-value) were computed with HOMER (*73*) using tissue-specific peaks and scaled to the top enriched tissue.

(F) UMAP plots of SMCs colored by gene accessibility (Top) and chromVar motif deviation scores (Bottom) for gonadal SMC markers *Wt1* and *Esr1*.

(G) The stacking bar plots show tissue composition per cluster for VECs (Left), FBs (Middle), and SMCs (Right). The dot plots show aging-associated proportional changes of clusters across tissues, colored by Pearson correlation between cluster proportion (normalized per tissue) and age. Clusters with significant age/age-sex effects are annotated (p-adjusted < 0.05).

(H) UMAP of VECs colored by the accessibility of VEC-5 markers (*Meox2*, *Lhx6*, *Slc7a14*).

(I) Scatterplots showing the age-related decline in VEC-5 proportions in muscle (quadriceps), gonadal white adipose tissue (gWAT), and ovary/uterus.

(J) UMAP of FBs colored by the accessibility of FB-18 markers (*Ifi207*, *Ear1*).

(K) Scatterplots showing the age-associated increase in FB-5 proportions in mesenteric WAT (mWAT), stomach, cecum, and esophagus.

(L) UMAP plot showing gWAT VEC cells isolated from snRNA-seq data (*7*), colored by *Lhx6* expression (VEC-5 marker).

(M) Scatterplot showing age-dependent reduction in *Lhx6*+ gWAT endothelial cells.

Age- and sex-dependent epigenetic signatures of aging

We next investigated the organism-wide epigenetic aging program by examining 349 organ-specific main cell types. For each major cell type in each tissue, we performed differential accessibility (DA) analyses in females and males separately (**Methods**). From these analyses, we identified both shared and sex-specific age-associated alterations in chromatin accessibility. We then carried out linkage analysis to map downstream genetic targets of these chromatin sites and examined upstream regulators by assessing the activity of intrinsic transcription factors and extrinsic cytokine signaling pathways that drive epigenetic reprogramming during mammalian aging (**Fig. 6A**).

In total, we identified 1,318,007 and 959,361 cell-type-specific and aging-associated DA peaks in females and males, respectively (**Fig. 6B, Fig. S10A, Table S6-S8**). While the number of DA peaks generally correlated with cell numbers, a few cell types exhibited notably strong aging-related chromatin changes, standing out as outliers with high regression residuals—such as B cells from brown adipose tissue or kidney, tenocytes, and muscle satellite cells (**Fig. S10B**). Among the identified DA peaks, a total of 540,386 cell-type-specific DA peaks were present in both sexes, most (96.9%) exhibiting consistent changes in the same cell type across both males and females (Spearman correlation of log transformed fold change = 0.86, p-value < $2.2 * 10^{-16}$, **Fig. 6C-D**).

While many DA peaks were restricted to only a few cell types (91.4% found in no more than 3 cell types), we also uncovered a subset of peaks (n = 803) that were consistently altered across many cell types (n >= 10) and tissues (**Fig. 6E**). This subset highlights coordinated chromatin dynamics across diverse cell types and regions during mammalian aging. Notable examples include increased promoter accessibility of the mineralocorticoid receptor *Nr3c2* (in 63 cell types, **Fig. 6F-G, left**) and the proinflammatory cytokine *Il7* (in 26 cell types, **Fig. 6F-G, middle left**), predominantly within immune cells. Increased *Nr3c2* activity also marked the aging-associated B cell states (**Fig. 4B**). Conversely, we identified DA peaks with decreased accessibility in aging, such as promoters of *Sox4* (in 25 cell types) and *Sox11* (in 19 cell types)(**Fig. 6E**). Specifically, *Sox11*, a transcription factor involved in angiogenesis (*74*), showed reduced accessibility in endothelial cells across multiple organs (**Fig. 6F-G, middle right**), which could contribute to the global functional decline of the vascular system.

Aging-associated chromatin alterations were not always uniform across cell types. For example, 131 peaks showed opposite changes in different cell types (at least five cell types in each direction). One example is a peak in the intron of *Epha3*, which displayed increased accessibility in T cells and macrophages across 12 tissues but decreased accessibility in non-immune cell types such as vascular cells, neurons, and epithelial cells (**Fig. 6F-G, right, Fig. S10C**). These cell-type-specific patterns were confirmed across both sexes (**Fig. 6F**), suggesting that aging-associated chromatin alterations are shaped by unique cellular contexts and lineage-specific regulatory networks.

These epigenetic changes in aging also vary by sex. Considering peaks with significantly increased accessibility in aging, we found 195,893 sex-specific peaks in females and 140,770 in males (**Fig. 6H**). Top female-specific DA peaks validated across multiple cell types from different tissues included intronic peaks at the senescence-associated gene *Cdkn2b* (in 18 cell types) and promoter peaks of the interferon-inducible gene *Ligp1* (in 14 cell types) and *Ifi211* (in 16 cell types) (**Fig. 6H**). Similarly, we observed male-specific DA peaks shared across multiple cell types, such as the increased promoter accessibility of *Tsbp1* across 18 cell types (**Fig. 6H**). We also identified cell-type-specific chromatin accessibility changes that were highly sex-dependent. For example, aged hepatocytes in females showed up-regulation of peaks overlapping with *Bnc2* (**Fig. 6I, left)**, a gene involved in extracellular matrix production and degradation

(*75*). In contrast, aged hepatocytes in males showed up-regulation of peaks overlapping with *Cidea* (**Fig. S6D, left**), a gene involved in lipid particle organizations. Similarly, in a subtype of proximal tubule cells segment 3 (PT S3T2), peaks overlapping *Mill2* were more accessible in aged females (**Fig. S6D, right**), whereas intronic peaks in *Tifa*—a gene associated with programmed cell death (*76*)—were more accessible in aged males (**Fig. 6I, right**). Consistent with these findings, this cellular state specifically declined in aged males (**Fig. 2H**). Notably, these sex- and cell-type-specific peaks were further validated by corresponding changes in promoter accessibility and gene expression during aging (**Fig. 6I-J and S6E**).

To infer putative target genes of aging-associated chromatin alterations in cis-regulatory elements (CRE), we linked non-promoter DA peaks to nearby promoters based on their co-accessibility across samples for each cell type, thus generating promoter-CRE linkages. We then integrated the data with a published snRNA-seq atlas of aging (*7*) to identify genes exhibiting consistent changes between promoters and expressions with age (**Methods**). This analysis identified 21,360 and 14,564 cell-type-specific gene-promoter-CRE linkages in males and females, respectively, with 12,862 linkages shared by both sexes (**Table S9**). In total, this revealed 15,090 CREs linked to aging-associated changes in 2,001 differentially expressed (DE) genes across 86 organ-specific cell types (**Fig. 6K**). Collapsing sex-shared, up-regulation linkages across cell types revealed concordant changes supported in three molecular evidences (i.e, genes, promoters and putative enhancers) (**Fig. 6L**). One notable example is *Nr3c2*, linked to 25 CREs, most located in intronic regions (**Fig. 6M**). These CREs showed strongly increased accessibility during aging across multiple immune cell types and tissues, in line with changes in promoter accessibility and gene expression from the same cell type (**Fig. 6N**).

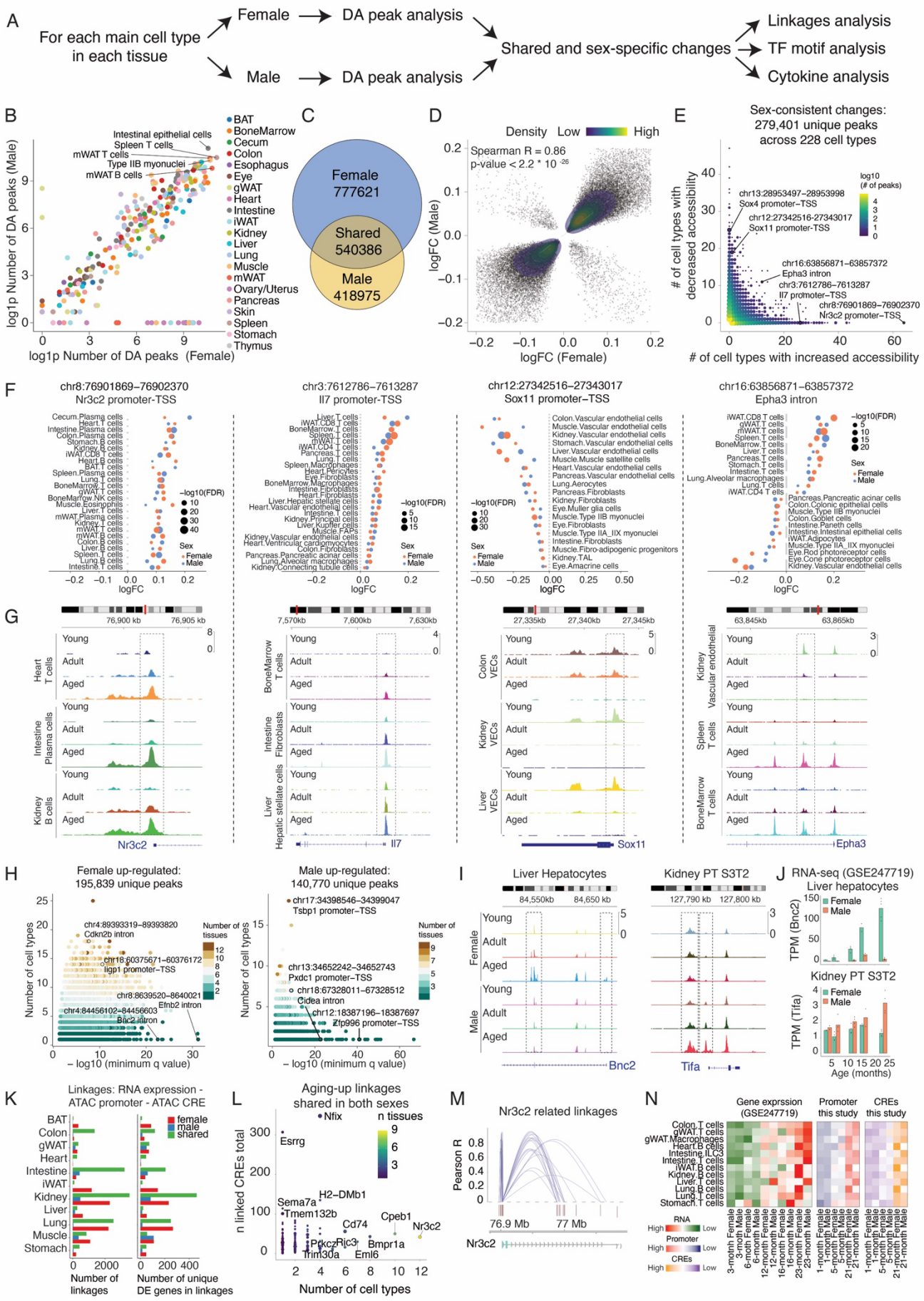

Figure 6. Aging-associated changes of chromatin accessibility.

(A) Scheme for computational analyses to identify differentially accessible (DA) peaks along aging, their putative gene targets, and upstream regulators.

(B) Scatterplot comparing the number of DA peaks between males and females for each main cell type. Cell types with a high number of DA peaks are labeled.

(C) Venn plot of cell-type-specific DA peaks shared or unique to males and females.

(D) Correlation of log transformed fold change (logFC, aging-associated accessibility changes per month, calculated via edgeR (*77*)) for DA peaks shared between sexes.

(E) Scatterplot summarizing DA peaks with concordant changes with aging in both sexes. Axes show counts of cell types with increased (x-axis) or decreased (y-axis) accessibility; color denotes peak density.

(F) Dot plots showing log transformed fold change (logFC) for DA peaks with consistent increases (promoters of *Nr3c2* and *Il7*), decreases (promoters of *Sox4*), or divergent trends (intronic peak of *Epha3*) across cell types.

(G) Genomic tracks visualizing the accessibilities of DA peaks in (**F**) across three age groups.

(H) Dot plots of sex-specific DA peaks for females (Left) and males (Right). Y-axis: number of cell types with significant increases; x-axis: -log10(q-value) for the most significant cell type. Color denotes the number of tissues with significant increases.

(I) Genomic tracks of female-specific DA peak in liver hepatocytes (Left) and male-specific DA peak kidney proximal tubule cells S3T2 (Right).

(J) Barplot showing validation of sex-specific chromatin accessibility changes using gene expression data (*7*) of the same genes in the same cell type as in (**I**). Dots represent gene expression of target genes across independent animals, quantified by transcripts per million (TPM).

(K) Barplot showing the number of cell-type-specific, aging-associated gene-promoter-CRE linkages (Left) and the number of unique genes within those linkages (Right) for each tissue.

(L) Dot plot of genes with aging-upregulated linkages in both sexes. X-axis: cell-type count; y-axis: CRE count per gene. Color denotes the number of tissues containing cell types with significant increases.

(M) Genome browser plot showing links between putative cis-regulatory elements and promoters for *Nr3c2*.

(N) Heatmaps showing coordinated increases in gene expression, promoter accessibility, and linked distal CRE accessibility of *Nr3c2* across multiple immune cells with aging.

We then explored upstream regulators of these aging-associated chromatin changes by performing motif enrichment analyses of DA peaks in each cell type. Aging-upregulated peaks were enriched for inflammatory motifs that are confirmed across multiple cell types, including IFN-stimulated response elements (ISRE) in 80 cell types, IRF1 in 77 cell types, IRF2 in 85 cell types, NF-κB in 57 cell types, and AP-1 in 71 cell types (**Fig. 7A-B**). In contrast, downregulated peaks were enriched for TF families linked to stem cell maintenance and development, such as *SOX15* (in 18 cell types) and *E2A* (in 29 cell types) (**Fig. 7A**). Sex-specific patterns also emerged. For example, female-specific upregulated peaks were enriched for *POU* motifs in B cells and male-specific upregulated peaks were enriched for inflammatory TF motifs (IRFs and AP-1) in intestinal epithelial cells (**Fig. 7C**).

These TF activity changes were further supported by corresponding gene expression dynamics observed in single-cell RNA-seq data. For example, in the aged B cells in the lung, we detected reduced motif accessibility for Ebf1 and Ets1 (**Fig. 7D-E**), transcription factors involved in B cell development (*25*) and quiescent state maintenance (*78*), aligning with their decreased expression in both sexes (**Fig. 7F**). Meanwhile, aged B cells exhibited decreased expression and increased motif accessibility for Irf2 (**Fig. 7D-E**), reflecting its role as a transcriptional repressor of inflammatory signaling (*79*, *80*). Pou2f2, a TF involved in B proliferation and plasma cell differentiation(*81*), showed increased motif accessibility exclusively in female-upregulated peak sets, corroborated by female-specific increases in Pou2f2 expression(**Fig. 7D-E**). This pattern is consistent with the preferential expansion of aging-associated B cells in female tissues (**Fig. 4D and 4H**). Moreover, the aging-associated changes in EBF and IRF motifs were detected in B cells body-wide, highlighting a global chromatin transition in B cells during aging (**Fig. 7G**).

Recognizing the strong inflammatory signature underlying these changes, we next explored whether cytokines known to drive immune responses could contribute to global epigenetic remodeling. Using the Immune Dictionary dataset (*82*), which encompasses scRNA-seq profiles of various immune cell types responding to 86 cytokines, we compared aging-related DA peaks and associated gene changes with those induced by different cytokines (**Fig. 7H, Methods**). This revealed that aging signatures, especially in female B cells from the lung, resembled those induced by specific cytokines such as interferons (IFNs), IL4, IL12, IL15, IL18, and IL21 (**Fig. 7I**). Cross-referencing aging-upregulated gene expression changes with cytokine-responsive transcripts further validated these links (**Fig. 7J**).

To reinforce this connection, we examined whether cytokine signatures were supported by changes in the accessibility of either secretion or receptor genes (**Fig. 7K-L**). For example, for secretion factors, we observed an increased accessibility of *Infg* and *Il21* in T cells, as well as *Il4* and *Il15* in B cells (**Fig. 7L**), aligning with activation of corresponding signatures, particularly in females (**Fig. 7I**). On the other hand, the upregulated response to IL2 and IL15 matched with increased accessibility of the receptor gene, *Il2rb*, in the aged B cells (**Fig. 7L**). A consistent trend was observed by analysis of recent snRNA-seq data (*7*), such as the increased expression of *Il21* in T cells, *Il2rb* and *Il15* in B cells (**Fig. 7N** and **Fig. S10F**).

Extending this analysis to all B cells across tissues uncovered the widespread emergence of cytokine signatures associated with aging, especially IL2, IL15, IFNγ, IL4, and IL21(**Fig. 7M**). Notably, the upregulated IL21 signatures were consistent with the global expansion of *Il21*+ T cells from in our previous analysis (**T cells - 9, Fig. 4B and 4D**) and were further confirmed at the plasma protein level in humans (*3*)(**Fig. S10G**). Interestingly, a previous study has described the function of IL21 in inducing the expression of Tbx21 (a marker of aging-associated B cells, **Fig. 4B**) in B cells and promoting their differentiation into

plasma cells in systemic lupus erythematosus (*83*), suggesting a potential similar role of *Il21* in the epigenome reprogramming of B cells during aging. Similarly, we analyzed cytokine signatures in macrophages by leveraging expression changes following cytokine treatments of the same cell type from Immune Dictionary. This revealed activation of a distinct set of cytokines, including IL15, IL7, IL1α, IL18, and TNFα (**Fig. S10H**), that may underlie age-related molecular shifts in macrophages.

In summary, our integrative multi-level framework reveals a global, sex-dependent epigenetic reprogramming linked to inflammatory signaling and cytokine-driven pathways. These findings provide a roadmap for understanding the regulatory underpinnings of aging across diverse cell types and tissues—from intrinsic TF regulators to extrinsic cytokine signaling—and highlight candidate upstream factors that could be targeted to mitigate age-related epigenetic dysregulation.

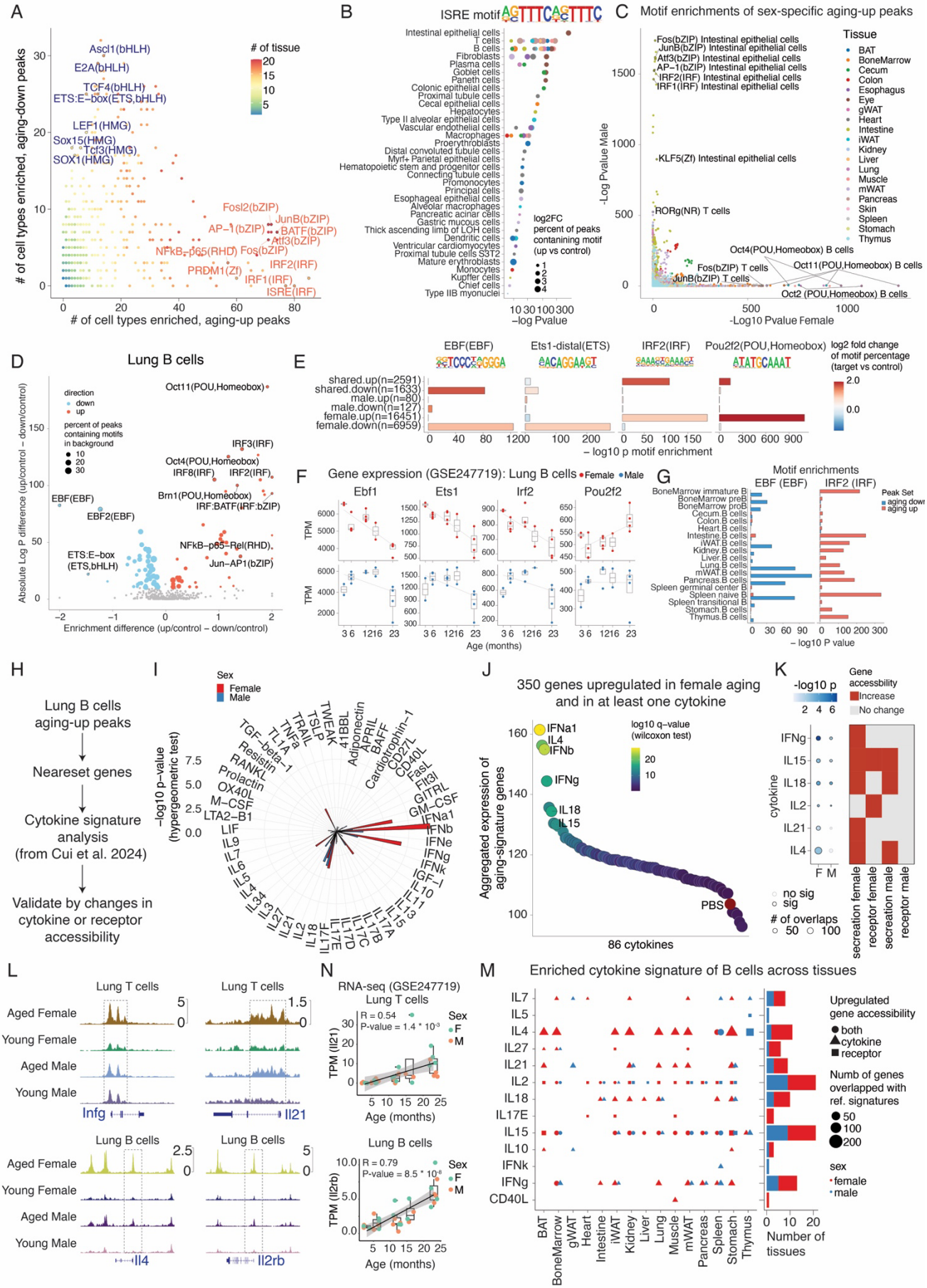

Figure 7. Identifying upstream regulators of aging-associated chromatin changes.

(A) Sex-shared aging-associated up-regulated and down-regulated differentially accessible (DA) peaks for each main cell type were analyzed for transcription factor (TF) motif enrichment using HOMER (*73*). The scatter plot summarizes the number of cell types exhibiting significant motif enrichments (p.adj < 0.05) in either up-regulated (red) or down-regulated (blue) peak sets. TF motifs enriched across multiple cell types are labeled.

(B) Dot plot showing the enrichment of interferon-stimulated response element (ISRE) motifs in aging-up DA peaks across cell types from diverse tissues. Dot size represents the fold change in ISRE-containing peaks in DA sets compared to a background peak set (**Methods**). Each dot represents one cell type from a specific tissue, colored by the tissue of origin.

(C) Comparison of TF motif enrichment significance between female-specific and male-specific aging-up peak sets for each main cell type. Cell types with strong sex-specific motif enrichments are labeled.

(D) Scatter plot showing enriched TF motifs in sex-shared, aging-up (red), and aging-down (blue) peaks from lung B cells. The x-axis denotes the difference in motif frequency (%) between DA and background peaks; the y-axis represents statistical significance.

(E) Barplots showing motif enrichment for exemplary TFs: Ebf1 and Ets1 (down-regulated in both sexes), Irf2 (up-regulated in both sexes), and Pou2f2 (female-biased up-regulation) in lung B cells.

(F) Scatterplot and barplot showing age-related expression changes of TFs highlighted in (**E**) in lung B cells, quantified using transcripts per million (TPM) for each animal.

(G) Enrichment significance of EBF and IRF motifs for DA peaks from B cells across tissues, demonstrating conserved aging-associated regulatory patterns.

(H) Scheme for computational analyses to identify cytokines potentially drive aging-associated chromatin remodeling in lung B cells.

(I) Circle plot showing enrichments (-log10(p-value), hypergeometric test) of cytokine-specific signatures (derived from Immune Dictionary dataset (*82*)) in aging-associated genes identified in lung B cells from this study.

(J) Dot plot displaying aggregated gene expressions of 350 genes shared between aging and cytokine treatments. Top conditions recapitulating aging-associated expression profiles were labeled.

(K) Left: dot plot showing the enrichment score (-log10(p-value), hypergeometric test) of cytokine signatures in the male and female lung B cells as in **(I)**. Right: Heatmap indicating the aging-associated changes in the accessibility of cytokine secretion or receptor genes.

(L) Genomic tracks showing aging-associated accessibility increases at *Ifng* and *Il21* in lung T cells and *Il4* and *Il2rb* in B cells.

(N) Scatterplot showing increased gene expressions of *Il21* in T cells and *Il2rb* in B cells with age, together with a linear regression line.

(M) Left, dot plot summarizing the enriched cytokine signatures using aging-up peak sets of B cells from each tissue. Only signatures that can be supported by increased accessibilities of secretion or receptor genes are shown. Right: barplot summarizing the number of tissues with activated signatures for each cytokine, splitting males and females.

Discussion

Aging involves global deterioration in cellular and organismal function. While advancements in genomics techniques, especially single-cell RNA-seq and spatial transcriptomics, have been used to explore age-associated changes in cell-type- and region-specific gene expression (*15*, *57*, *84*, *85*), few studies have systematically investigated cell population shifts, chromatin dynamics, as well as age-sex interaction on the scale of the entire organism. Here, by profiling around seven million cells from 21 mouse tissues at three ages and in both sexes, we constructed a single-cell chromatin accessibility atlas of aging with unprecedented depth and breadth. We reported the aging-associated dynamics of 536 tissue-level main cell types and 1,828 finer-grained subtypes, each defined by the accessibility at approximately 1.3 million cis-regulatory elements. Our findings reveal widespread cell population shifts, lineage-specific epigenomic reprogramming, and striking sex-dependent patterns, laying a foundation for understanding the regulatory logic of mammalian aging.

A key insight of our study is the extensive cell population dynamics accompanying age. Notably, 146 organ-specific cell types (approximately 25% of all organ-specific cell types) changed significantly with age. Many of these are immune cells. For example, we observed a widespread increase in plasma cells and macrophages across various tissues, aligning with previous findings of immunoglobulin accumulation (*85*) and monocyte/macrophage propagation (*86*) in aging. Tissue-specific population changes, such as the expansion of neutrophils in the liver and lung, and depletion of lymphoid progenitors in primary immune organs (e.g., pre-/pro-B cells in the bone marrow and immature T cells in the thymus) were identified. Beyond immune-related changes, our study also reveals additional vulnerabilities in non-immune cell lineages. For example, we observed profound depletion of specialized functional cell types across multiple organs, such as kidney podocytes, muscle tenocytes and satellite cells, ovary granulosa cells, and lung aerocytes. These depletions likely contribute to age-related loss of tissue homeostasis and functions.

Beyond shifts in broad cell types, our high-resolution analysis identified 1,828 subtypes—nearly one-third of which show significant aging dynamics. We identified subtypes exhibiting cell state changes that diverge from their parent population. For example, naive T cell subtypes in the lung and liver sharply decline, although total T cell proportions rise with age. Likewise, we detected region-specific vulnerability of endothelial cells in the kidney medulla and vein, distinct expansions in fibroblast and mast cell subpopulations in the intestine, and the emergence of a shared reactive state (*Creb5*+ *Bnc2*+ *Runx1*+) across different epithelial cell types in the kidney. These findings suggest that aging promotes a variety of cell-state transitions, including those localized to particular anatomical niches or widespread across distinct parent cell types potentially triggered by common circulating factors.

Coordinated expansion or depletion of the same subtype in multiple organs underscores a broader organism-level program. Immune subtypes, in particular, display strikingly synchronous changes, such as the global expansion of *Gzmk*+ CD8 T cells, regulatory T cells, *Il21*+ CD4 T cells, *Il23r*+ innate T cells and *Tbx21*+ B cells. Certain changes were restricted to a few organs, including the depletion of *Zfp683*+ tissue-resident memory T cells in adipose and gut tissues, or the decline of *Gzma*+ resting NK cells in spleen and bone marrow. However, this synchronization extends beyond mobile immune lineages: certain endothelial and fibroblast populations, also show parallel shifts across distinct tissues, such as the depletion of *Slc7a14*+ *Lhx6*+ *Meox2*+ vein endothelial cell and the expansion of an *Ifi207*+ *Ear1*+ aging-associated fibroblast subtype. This points to systemic inflammatory signals or hormonal cues that modulate cell fates body-wide.

At the molecular level, we identified extensive chromatin reprogramming associated with aging. Our differential accessibility analyses uncovered 279,401 peaks changing with age, including a subset consistently altered across many cell types (e.g., promoter peaks of *Nr3c2* and *Il7* that frequently gain accessibility, and *Sox4* or *Sox11* peaks that frequently lose accessibility). Linking chromatin changes to RNA-seq data validated the effects from accessibilities to expressions and revealed putative enhancers regulating aging-associated genes. Motif analysis further supports a shift from TFs involved in tissue maintenance or stemness (*e.g., SOX, E2A*) to those mediating inflammatory and stress responses (*e.g., NF-κB, IRFs, AP-1*). Specifically, as an example to showcase the potential of our data to reveal anti-aging targets, we focused on cytokines and identified the activation of IL15, IL21, IL4, and IFNγ signatures in aged B cells, indicating these extrinsic signals may reinforce or drive the cell-state transitions observed in aging.

Crucially, we found extensive sexual dimorphism. Around forty percent of aging-associated main cell types (55 out of 146) and subtypes (193 out of 499) exhibited sex differences. Notable examples include the male-biased expansion of hepatic stellate cells in the liver and the female-biased expansion of interstitial macrophages in the lung. Overall, female mice appeared to mount a more pronounced immune activation in aging at both proportional and molecular levels, consistent with the higher incidence of autoimmune diseases in women (*87*, *88*). This included female-specific upregulation of TFs like *Pou2f2* in B cells, aligning with female-biased expansions of aging-associated B cell subtypes. We also observed subtypes that shift in opposite directions by sex, such as *Slc22a7*+ proximal tubule cells (PT S3T2) increasing in aged females but decreasing in males—trends replicated by single-cell transcriptomic data. At the epigenetic level, we detected tens of thousands of cell-type-specific peaks that changed exclusively in one sex, highlighting sex as a major axis of aging heterogeneity.

In summary, this organism-level single-cell chromatin accessibility atlas illuminates how aging remodels the cellular composition and regulatory landscape of multiple tissues. Although many changes are highly tissue-specific, we uncovered “coordinated” cellular and molecular dynamics that are shared across different organs, including immune remodeling, broad depletion of functional cell types, the emergence of inflammation-related states, and sex-dependent trajectories. By cataloging these changes, we offer a resource for understanding the molecular logic of aging and for guiding therapeutic strategies aimed at preserving or restoring youthful tissue states. This work also highlights molecular candidates to mitigate aging-related dysfunction by targeting broad-spectral cell types across tissues, including intrinsic transcription factors, extrinsic cytokines, and individual receptors (*Nr3c2* for immune cells, *Epha3* for T cells, *Il2rb* for B cells). Looking forward, we anticipate that this atlas will serve as a critical reference for evaluating anti-aging interventions and refining our understanding of how chromatin remodeling, cell state transitions, and tissue physiology intersect in the aging mammalian body.

Acknowledgments

We thank members of the Cao lab for helpful discussions and feedback. We also thank members of the Rockefeller University High-Performance Computing Core, Comparative Bioscience Center, Genomics Resource Center, Bioinformatics Resource Center and Flow Cytometry Resource Center for their invaluable support.

Funding: This work was funded by grants from NIH (DP2HG012522, R01AG076932, and RM1HG011014 to J.C.), the Sagol Network GerOmic Award and Hevolution/AFAR New Investigator Awards in Aging Biology for J.C.. W.Z. was funded by the SNF RU Institute for Global Infectious Disease Research and Kellen Women's Entrepreneurship Fund. The project was supported by a Longevity Impetus Grant from Norn Group.

Author contributions: J.C. and W.Z. conceptualized and supervised the project; Z.L. optimized nuclei extraction methods and EasySci-ATAC protocols; Z.L. performed mouse dissection, nuclei extraction, and single-cell ATAC-seq experiment; Z.L. performed all computational analyses with insights from Z.X, Z.Z, and A.A.; J.C., W.Z., and Z.L. wrote the manuscript with input from all co-authors.

Competing interests: J.C., W.Z., and Z.L. are inventors on a patent application (U.S. 63/377,061) submitted by Rockefeller University that covers the methods for *EasySci* development.

Data availability: Raw FASTQ files, processed count matrices, cell metadata, and peak metadata can be downloaded from NCBI GEO under accession number GSE288730 (reviewer's token: exitcckgbfmzpkl). An interactive website facilitating the visualization of our data across cell type, age, and sex is available at https://mouseagingatacatlas.org.

Code availability: Custom code and scripts used for processing sequencing reads of EasySci-ATAC-seq library were deposited in Zenodo (*89*) (https://doi.org/10.5281/zenodo.8395492) .

Supplementary Materials

Materials and Methods:

Animals and organ collection

The C57BL/6 wild-type mice at one month (n=10, 5 males and 5 females), five months (n=10, 5 males and 5 females), and twenty-one months (n=12, 6 males and 6 females) were obtained from The Jackson Laboratory. Detailed information on animal individuals in this study is provided in Table S1A. Mice were housed socially and maintained on a regular 12h/12h day/night cycle. In order to analyze newborn cells from the same set of samples in parallel, all mice were labeled with EdU (25 mg/kg, i.p. injection) at 24-hour intervals for five days. Tissues were harvested one day after the final injection. To control for circadian effects, sample harvest was performed around the same period (4-7 PM) across all individuals. Mice were euthanized utilizing inhalation of carbon dioxide (CO2). After euthanization, major organs were quickly transferred into ice-cold PBS, and the following tissues were collected: brown adipose tissue, bone marrow, cecum, colon, esophagus, eye, heart, small intestine (spanning duodenum, jejunum, and ileum), kidney, liver, lung, muscle (quadriceps and gastrocnemius), ovary and uterus, pancreas, back skin, spleen, stomach, thymus, gonadal white adipose tissue, inguinal white adipose tissue, mesenteric adipose tissue. Dissected mouse tissues were snap-frozen in liquid nitrogen and stored at -80C. All animal procedures were in accordance with institutional regulations under the IACUC protocol 21049.

Nuclei extraction from multiple mammalian organs

Nuclei extraction was performed using the method from (*90*) and (*7*) with slight modifications. Before extraction, frozen tissues were placed inside aluminum foil, and smashed into powders on dry ice with a hammer. 10X PBS-hypotonic stock solution was prepared as follows: 6.83 g of Na_2HPO_4-$2H_2O$ (Sigma, 71643-250G), 3.5 g of NaH_2PO_4-H_2O (CATALOG), 1.2 g of KH_2PO_4 (Sigma, P285-500), 1 g of KCl (Sigma, P9541-1KG) and 3 g of NaCl (Sigma, P9888-500G) in nuclease-free water to a final volume of 500 mL. On the day of nuclei extraction, 1X nuclei lysis buffer was prepared freshly as follows: final concentration of 1X PBS-hypotonic stock solution, 3 mM $MgCl_2$ (VWR, 97062-848), 0.025% IGEPAL CA-630 (VWR, IC0219859650), 0.1% Tween-20 (Sigma, P9416-100ML), 1X cOmplete, EDTA-free Protease Inhibitor Cocktail (Sigma, 11873580001). In addition, a final concentration of 0.33M sucrose (Sigma, S0389) was included in the lysis buffer for these tissues: esophagus, stomach, intestinal, cecum, colon, spleen, thymus, bone marrow and skin. The powdered tissues were then transferred into 10-20 mL nuclei lysis buffer, followed by brief vortexing and incubation for 10-15 minutes at 4C on a rotator. Extracted nuclei were then filtered through 40 um cell strainers (VWR, 470236-276), stained with 4',6-diamidino-2-phenylindole staining (DAPI, Invitrogen D1306), and FACS sorted for singlets.

EasySci library construction and sequencing

The EasySci-ATAC library was prepared following the prior study (*15*), except for a few modifications. The sorted nuclei were pelleted down at 500g for 5 minutes, resuspend in nuclei buffer [10 mM Tris-HCl pH 7.5 (VWR, 97062-936), 10 mM NaCl (VWR, 97062-858), 3 mM $MgCl_2$ (VWR, 97062-848), 0.025% IGEPAL CA-630 (VWR, IC0219859650), 0.1% Tween-20 (Sigma, P9416-100ML), 1X cOmplete, EDTA-free Protease Inhibitor Cocktail (Sigma, 11873580001)] to a final concentrations of 1000~2000 nuclei/μL. Nuclei were mixed in a 1:1 ratio with 2X TD buffer [20 mM Tris-HCl pH 7.5, 20 mM $MgCl_2$, 20% Dimethylformamide (Fisher, AC327175000)] and dispensed 10 μL into each well of four 96-well plates. 1 μL barcoded Tn5 was

loaded into each well. Tagmentation reaction was performed at 37°C for 30 minutes with gentle shaking at 300 rpm and stopped by adding 11 µL of 2X Stop buffer [40 mM EDTA (VWR, 37062-656), 1 mM Spermidine (Sigma, S0266-1G)] to each well. Samples were pooled and washed twice and resuspended resuspended in nuclei buffer. 5 µL of resuspended nuclei were distributed into each well of 96-well plates. 2 µL indexed EasySci P5 ligation adapters and 3 µL ligation mix [1 µL nuclease-free water, 1 µL 10X T4 DNA ligase buffer, 1 µL T4 DNA ligase (NEB, M0202L)] were added to each well. Ligation was performed at room temperature for 30 minutes with medium-speed rocking (350g) and stopped by adding 2 µL of 18 mM EDTA to each well. After that, nuclei were pooled, washed, resuspended using nuclei buffer, and subjected to another round of FAC sort based on DAPI staining to remove doublets. Then, sorted nuclei were distributed into PCR plates as 5 uL per well. Proteinase K treatment was performed by mixing each well with 0.25 µL 18.9 mg/mL proteinase K (Sigma, 3115828001), 0.25 µL 1% SDS, and 0.5 µL EB buffer, and plates were incubated at 65°C for 16 hours. Then, 2 µL 10% Tween-20 was added to each well to quench the SDS. Following on, 1 µL of 10 µM universal P5 primer (5′-AATGATACGGCGACCACCGAGATCTACAC-3′, IDT), 1 µL of 10 µM indexed P7 primer (5'-CAAGCAGAAGACGGCATACGAGAT[i7]GTGACTGGAGTTCAGACGTGTGCTCTTCCGATCT-3', IDT) and 10 µL NEBNext High-Fidelity 2X PCR Master Mix (NEB M0541L) were added into each well. Amplification was carried out using the following program: 72°C for 5 minutes, 98°C for 30 seconds, 13-14 cycles of 98°C for 10 seconds, 66°C for 30 seconds, 72°C for 30 seconds and a final 72°C for 5 minutes. Final PCR products were pooled and purified by column purification using a Zymo DNA Clean & Concentrator kit (Zymoresearch, D4014) followed by gel extraction using Zymoclean Gel DNA Recovery Kit (Zymoresearch, D4007) to remove adapter dimers. Library concentrations were determined by Qubit and the libraries were visualized by electrophoresis on a 2% E-Gel™ EX Agarose Gels (Invitrogen G402022).

Processing of sequencing reads

Base calls were converted to fastq format and demultiplexed using Illumina's bcl2fastq/v2.19.0.316 tolerating one mismatched base in barcodes (edit distance (ED) <= 1). Then, indexed Tn5 barcodes and ligation barcodes were extracted, and corrected to their nearest barcode (edit distance (ED) <= 1). Reads with uncorrected barcodes (ED >= 2) were removed. Tn5 adaptors were removed from 5'-end and clipped from 3'-end using trim_galore/0.4.1 (https://github.com/FelixKrueger/TrimGalore). Trimmed reads were mapped to the mouse genome (mm10) using STAR/v2.5.2b with default settings. Aligned reads were filtered using samtools/v1.4.1 to retain reads mapped in proper pairs with quality score MAPQ > 30 and to keep only the primary alignment. Duplicates were removed by picard MarkDuplicates/v2.25.2 per PCR sample. Deduplicated bam files were converted to bedpe format using bedtools/v2.30.0, which were further converted to offset-adjusted (+4 bp for plus strand and -5 bp for minus) fragment files (.bed). Deduplicated reads were further split into constituent cellular indices using the Tn5 and ligation barcodes, and sparse matrices counting reads overlapping with promoter regions (±1 kb around transcription start site) were generated for quality filtering. In the meantime, fragment files were used to generate h5ad files for all downstream analyses with the snap.pp.import_data() function of SnapATAC2/v2.5.1. Cell-by-bin matrices were also generated with SnapATAC2 function snap.pp.add_tile_matrix() containing insertion counts across genome-wide 5000-bp bins.

Cell filtering, dimensionality reduction, clustering, and annotations

The following analyses were performed on the dataset of each tissue separately. After initial processing, cells with less than 1000 unique reads or less than 15% of reads in promoter regions were discarded. The

promoter ratio cutoff was adjusted to 0.1 for the eye dataset due to the observation of a lower promoter ratio in corneal epithelial cells. Then, we used an iterative clustering strategy to detect potential doublet cells from each organ, similar to our previous study (*15*, *91*). Briefly, doublet scores were calculated for each cell using SnapATAC2 function snap.pp.scrublet(). Meanwhile, all cells of each organ were subjected to clustering and sub-clustering analysis with spectral embedding and graph-based clustering implemented in SnapATAC2. Cells labeled as doublets (defined by a doublet probability cutoff of 0.5) or from doublet-derived sub-clusters (defined by a doublet ratio cutoff of 0.2) were manually examined and filtered out. We then generated gene activity matrices for each organ by counting the Tn5 insertions in the TSS and gene body regions for each gene using SnapATAC2 function snap.pp.make_gene_matrix(). Gene activity matrices were then used for cell type annotations.

To identify clusters of cells corresponding to different cell types, we subjected cells after data cleaning to dimension reduction and Leiden clustering using SnapATAC2 functions snap.tl.spectral(), snap.pp.knn() and snap.tl.leiden() with the default setting. UMAP coordinates were calculated based on the spectral embedding matrices using the function UMAP() with min_dist=0.01 from the Python package umap/v0.5.2 (*92*). For cell annotations, we first obtained a draft of annotations by integrating our chromatin data (subsampled to 2,000 cells per Leiden cluster) with the published sn-RNA-seq datasets (*7*) through Seurat/4.3.0.1 (*7*, *93*) label transfer, and we manually reviewed and refined the annotations for each Leiden cluster based on accessibilities of known markers listed in Table S2.

Peak calling

After cell annotation, reads from each main cell type of each tissue were concatenated. Then, Tn5-corrected single-base insertions were extracted and subjected to peak calling using macs3/v3.0.0b3 (*94*), with the following parameters: --nomodel --extsize 200 --shift -100 -q 0.1. Peak summits were extended by 250bp on either side and then merged iteratively, similar to (*12*). Specifically, the peak with the smallest p-value was kept and any peak that directly overlapped with it was removed. Then, this process was repeated to the second most significant peak and so on until all peaks were either kept or removed. Interactive merging was performed first across main cell types within each tissue, and then across all tissues to generate the universal peak set across the entire organism. The peak count matrices were generated using the SnapATAC2 function snap.pp.make_peak_matrix(). Peak annotations were performed using the HOMER function annotatePeaks.pl.

Identifications of cell-type-specific peaks

We used a Shannon entropy-based method to identify cell type-specific peaks, similar to previous studies (*12*, *95*). Starting from 144 unique cell types collapsed from all tissues, we first aggregated the peak count matrix for each cell type and normalized the aggregated matrix to counts per million (CPM). We then converted the CPM values into probabilities by dividing each cell type's CPM by the total CPM across all cell types for a given peak: $p_i = q_i / \Sigma q_i$, where "q_i" is the CPM value of the i-th cell type of a given peak. Next, we calculated Shannon entropy for each peak, which measures how uniformly accessibility is distributed across cell types: $H = - \Sigma (p_i * \log(p_i))$ where "p_i" is the probability of the i-th cell type for a given peak. To determine statistical significance, we generated a background distribution of entropy values using a set of peaks with low variability. Specifically, for each peak, we calculated the fold change between the most accessible cell type (quantified by CPM) and the average accessibility across all cell types. We then grouped peaks based on their mean accessibility into thirty bins. Within each bin, peaks with fold-change values below the 25th percentile were considered low-variable peaks, while those in the top 25th

percentile were considered high-variable peaks. The entropy threshold was set at a p-value of 0.05, using the low-variability peaks as the background. Cell type-specific peaks were identified from the high-variable peak set if their entropy values fell below this threshold. Cell-type-specific peaks, along with their maximum and average accessibility values quantified by CPM, can be found in Table S3.

LDSC analysis

To estimate enrichments of heritability for human traits in cell-type-specific peaks, we applied LDSC (*96*), which takes summary statistics from a given GWAS as input and quantifies the enrichment of heritability in an annotated set of SNPs conditioned on a baseline model that accounts for the non-random distribution of heritability across the genome. The LDSC computational pipeline was modified from (*97*) and the LDSC tutorial (https://github.com/bulik/ldsc/wiki/Cell-type-specific-analyses). Specifically, we first used the UCSC utility liftOver to lift all GWAS SNPs from the human to the mouse genome. We then took the top 2000 differentially accessible peaks per main cell type identified from the entropy-based method, and annotated each SNP according to whether or not it overlapped these cell-type-specific peaks. We then followed the recommended workflow for running LDSC using HapMap SNPs, precomputed files corresponding to 1000 genomes phase 3, excluding the MHC region to generate an LDSC model for each chromosome and peak set. GWAS summary statistics were obtained from the Broad LD Hub (https://data.broadinstitute.org/alkesgroup/sumstats_formatted/) and from GWAS catalogs (*98*) (https://www.ebi.ac.uk/gwas/downloads/summary-statistics). Coefficient P values calculated from LDSC were corrected for multiple hypotheses for each trait using the Benjamini-Hochberg method.

Identifications of sex dimorphism for main cell types

To examine cell types with sex dimorphism in chromatin accessibility profiles, we trained k-nearest neighbor (KNN) classifiers to distinguish male and female cells of the same age for each main cell type using python package sklearn/v1.0.2. Spectral embeddings generated from SnapATAC2 were used as input features to predict the sex of individual cells. Datasets were filtered to include only cell types with at least 200 total cells and a minimum of 50 cells per sex. We performed five independent train-test splits, using 80% of the data for training and 20% for testing, with stratified sampling to maintain sex balance. To ensure computational efficiency, we subsampled both training and test sets to a maximum of 2000 cells per cell type. Classification performance was evaluated using area under the curve (AUC) metrics, with cell types exhibiting AUC > 0.9 considered to display strong sex-associated chromatin differences.

Sub-clustering analysis

Sub-clustering analysis was performed using SnapATAC2, same as main clustering. Briefly, we subjected cells of the same type within the same tissue to feature selection (n_features=50000), dimension reduction and leiden clustering (resolution=1.5). UMAP coordinates were calculated based on the spectral embedding matrices (min_dist=0.01). We then examined the resulting Leiden clusters and manually merged those that overlapped in UMAP space without clear differences in gene accessibility. For certain cell types with pronounced sex dimorphism, including liver hepatocytes, kidney proximal tubule cells, type IIB myonuclei in muscle, adipocytes, and adipose stem and progenitor cells from gonadal white adipose tissue, sub-clustering was performed separately for males and females to capture cell-state differences rather than sex-based differences.

Differential Abundance Analysis

For each mouse individual, we quantified the proportion of each main cell type or subtype within each tissue, and applied a linear regression model (proportion ~ age + age:sex) to assess age-associated population dynamics while accounting for sex effects. The analysis was conducted using the R function lm(). Quadriceps and gastrocnemius muscles were analyzed separately, as they were from distinct anatomical locations. In the model, age was treated as a continuous variable (in months), while sex was considered a binary categorical variable. To identify significantly changing subtypes, we filtered results based on the following criteria: $R^2 > 0.4$ and a q-value (for either the age term or the age:sex interaction term) < 0.05. Multiple hypothesis correction was performed separately for each tissue using the Benjamini-Hochberg method. Additionally, Pearson correlation coefficients were calculated between the proportion of each main cell type or subtype and age. Based on these correlations, cell types and subtypes were classified into three groups: aging-up (q-value of the age term < 0.05, q-value of the age:sex interaction > 0.05, Pearson r > 0), aging-down (q-value of the age term < 0.05, q-value of the age:sex interaction > 0.05, Pearson r < 0), interaction-significant (q-value of the age:sex interaction < 0.05).

Differential Peak Analysis

In order to reduce the search space for differential peak analysis, we first selected highly accessible and highly variable peaks for each main cell type. First, the accessibility levels of all 1.3M peaks for each condition were quantified by counts per million (CPM) after aggregating data of the same age. Peaks were then ranked based on their CPM value in the most accessible condition, and only those above the 75th percentile were retained for each main cell type. These highly accessible peaks were further grouped into thirty bins based on their maximum accessibility. Within each bin, peaks with fold-change values (max condition vs. mean of three age groups) in the top 25th percentile were classified as highly variable peaks. This preselection was conducted separately for males and females, and the resulting peaks were collapsed across sexes.

Pre-filtered peaks for each main cell type were then analyzed for differential accessibility using edgeR/v3.36.0 (*12*, *77*). The analysis was performed at the pseudo-bulk level by aggregating single-cell peak counts from the same mouse sample, treating each individual mouse as a replicate. Age was treated as a continuous variable (in months). Only cell types with more than 200 cells in all three age groups were included in the analysis. Additionally, male and female samples were tested separately, with log fold-change (logFC), p-values, and q-values computed for each sex independently using edgeR. Differentially accessible peaks were categorized as follows: sex-shared, aging up-regulated peaks (p-value-female < 0.05 and p-value-male < 0.05, q-value-male < 0.05 or q-value-male < 0.05, logFC-female > 0, logFC-male > 0); sex-shared, aging down-regulated peaks (p-value-female < 0.05 and p-value-male < 0.05, q-value-male < 0.05 or q-value-male < 0.05, logFC-female < 0, logFC-male < 0); female-specific DA peaks (p-value-male > 0.05, q-value-female < 0.05); male-specific DA peaks (p-value-female > 0.05, q-value-male < 0.05).

Identifying aging-associated linkages of genes, promoters and cis-regulatory elements

This analysis aims to identify links between cis-regulatory elements and their putative target genes, and to validate accessibility changes with gene expression data. First, we focused on aging-associated differentially accessible (DA) peaks identified previously. Pearson correlation coefficients were computed between DA promoters and nearby non-promoter DA peaks (±500 kb) across samples, after pseudo-bulking each mouse individual. A background distribution was also generated by pairing DA promoters

with randomly selected peaks, and a threshold of Pearson correlation was defined with an empirical FDR = 0.05. The correlation analyses were performed separately for sex-shared, female-specific and male-specific peaks. In the meantime, we collected snRNA-seq data of mouse aging from (*7*), re-annotated the cells for consistent cell type labels between RNA-seq and ATAC-seq, and followed with differential gene expression changes using edgeR/v3.36.0 (*77*). Similar to differential accessible analysis, the differential expression analysis was performed separately for males and females in terms of each main cell type in each tissue, and at the pseudo-bulk level by aggregating single-cell gene counts from the same mouse individual. Differentially expressed genes, including sex-shared (p-value < 0.1 in both males and females, with the same logFC direction), female-specific (p-value < 0.1 in females but > 0.1 in males) and male-specific changes (p-value < 0.1 in males but > 0.1 in females) were defined. Finally, aging-associated linkages (gene-promoter-CRE) were defined if a gene exhibited consistent changes (up-regulated or down-regulated) in the same cell type from the same tissue across three layers, i.e, expression changes based on RNA-seq data, accessibility changes of promoters and non-promoter peaks based on ATAC-seq data, significant correlations between accessibilities of promoters and linked non-promoter sites.

Transcription factor motif analysis

We used Signac/v1.7.0 (*99*) and chromVAR/v1.16.0 (*21*) to quantify motif accessibility of transcription factors in Figure 3N, 5C, 5I, S3E, S3F and S7B. Position weight matrices of transcription factor binding sites were obtained from JASPAR2022 (*100*). A Signac object containing a peak count matrix of cells of interest was constructed using the Signac functions CreateChromatinAssay() and CreateSeuratObject(). Motif information was then added via AddMotifs(), and motif deviation scores were calculated for each single cell using RunChromVAR(). In Figure S3F, to compare motif activity and gene accessibility of transcription factors across cell types, motif deviation scores were rescaled to the range (0,10) using the R function rescale(), averaged per cell type, and scaled to z-score across cell types. In Figure 5C, motif footprinting analysis was performed using the Footprint() function in Signac.

For motif enrichment analysis of aging-associated differentially accessible (DA) peaks (Figure 7A, 7C, 7D, and 7E), we used the HOMER function findMotifsGenome.pl (*73*). A background peak set with minimal age-related changes was selected for each main cell type as a control for HOMER analysis. Specifically, accessible peaks for each cell type were grouped into thirty bins, based on accessibility in the highest condition. Within each bin, peaks with fold-change values (maximum condition vs. the mean of three age groups) in the bottom 10th percentile were classified as invariable peaks. The same background peak set was used to assess transcription factor motif enrichment across all aging-associated peak sets of a given cell type. Motif enrichments were quantified as the percentage of peaks containing a given motif in the target peak set relative to the background. Significance values (-log10 q-value) were calculated within HOMER.

Cytokine-related analysis

To evaluate the contribution of cytokine signaling to age-related molecular changes in B cells and macrophages, aging-upregulated DA peaks of each sex identified from chromatin accessibility data were first collapsed to their nearest genes using the HOMER function annotatePeaks.pl. The resulting gene sets (female-upregulated and male-upregulated) were compared to cytokine-induced gene sets of the same cell type from the Immune Dictionary Data (*82*). A hypergeometric test was performed using the R function phyper(). We only kept conditions containing more than ten DE genes after cytokine treatments identified from Immune Dictionary for this comparison.

As an additional measure of aging signatures across cytokine treatments, we overlapped the aging-upregulated gene signatures from our study with the union of genes that exhibited increased expression in at least one cytokine treatment. This overlapping gene set represents shared features between aging and cytokine responses. To identify cytokines that mimic aging phenotypes, we compared the aggregated expression of these genes across cytokine treatments to the PBS control. Statistical evaluation was conducted using Wilcoxon rank-sum tests (wilcox.test() in R).

To minimize cross-activation effects, we excluded cytokines whose receptors were not expressed (TPM < 1) in the target cell type, based on gene expression profiles from the Immune Dictionary. To further validate cytokine signaling changes and refine potential targets, we further analyzed chromatin accessibility changes in genes encoding cytokines and their receptors. Differential analyses were performed using gene accessibility matrices at the pseudo-bulk level, with females and males analyzed separately.

Finally, cytokine signatures were defined based on the following criteria: significant overlap with aging-peak-associated genes (p-value < 0.05, hypergeometric test); significant aging-mimicking activation compared to PBS (p-value < 0.05, Wilcoxon rank-sum test); can be supported by increased chromatin accessibility of the underlying genes in at least one cell type within the same tissue, or from increased chromatin accessibility of receptor genes in the target cell type.

Supplementary figures

Figs. S1 to S10

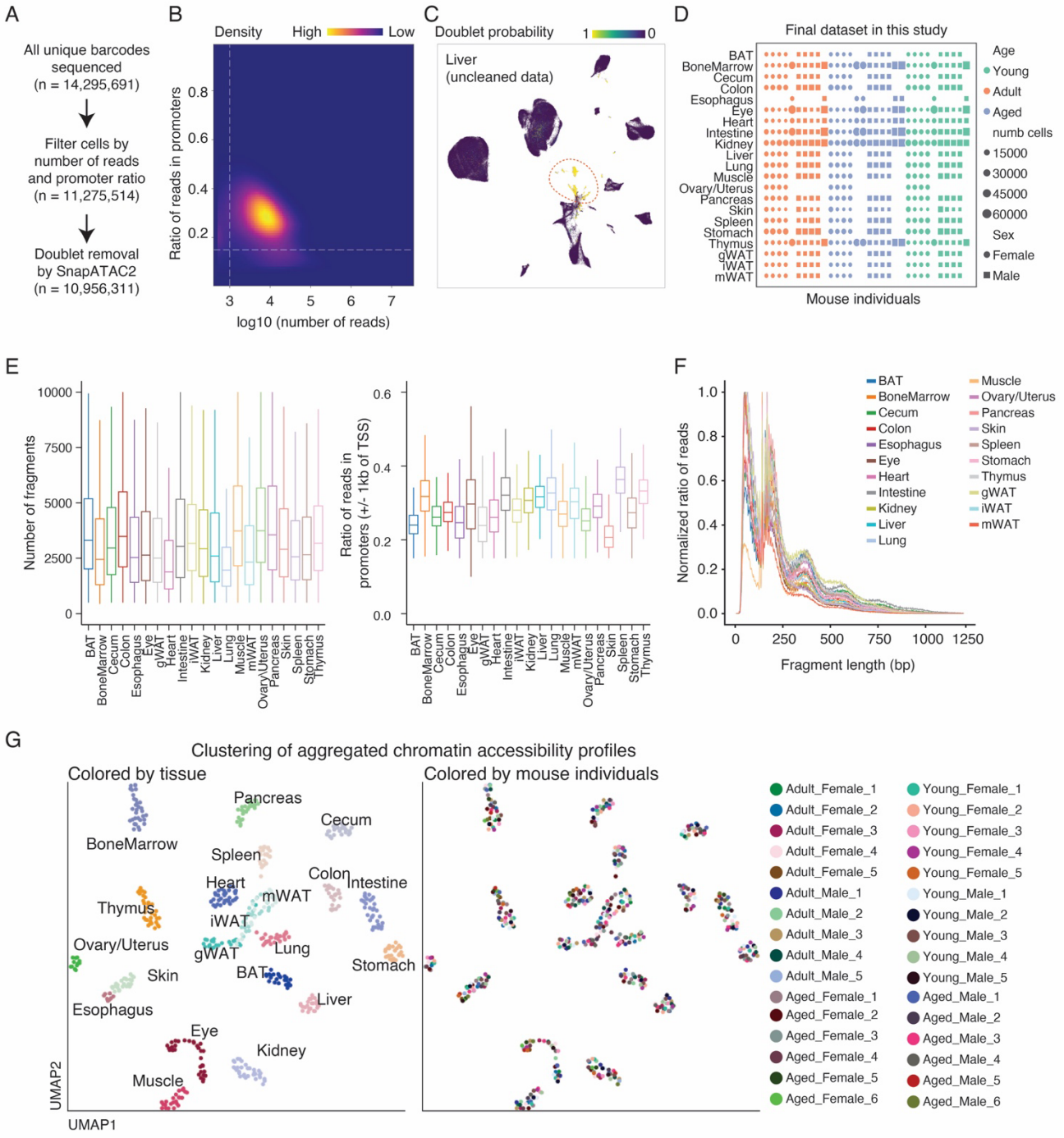

Figure S1. Overview of dataset quality.

(A) Scheme of data cleaning procedures. All sequenced cells underwent initial filtering determined by reads number and promoter ratio, followed by doublet removal using a modified pipeline based on SnapATAC2 (*17*).

(B) Density plot showing the distribution of the number of reads per nucleus versus the ratio of reads in promoters. Dash lines indicated cutoffs used for filtering (promoter ratio > 0.15 and > 1,000 unique reads).

(C) An example UMAP plot showing all liver cells (before doublet removal), colored by doublet probability. Circle indicated doublet cells.

(**D**) Dot plot showing the total number of cells obtained from each mouse individual after all quality control filterings.

(E) Box plot showing the number of fragments (left) and the ratio of reads mapped to promoters (± 1kb of TSS, right) per nucleus across tissues.

(**F**) Line plot showing the fragment length distributions of aggregated single cell ATAC-seq data across tissues.

(G) UMAP visualization of the aggregated chromatin accessibility profiles from all samples across tissues, colored by organ (left) and mouse individuals (right).

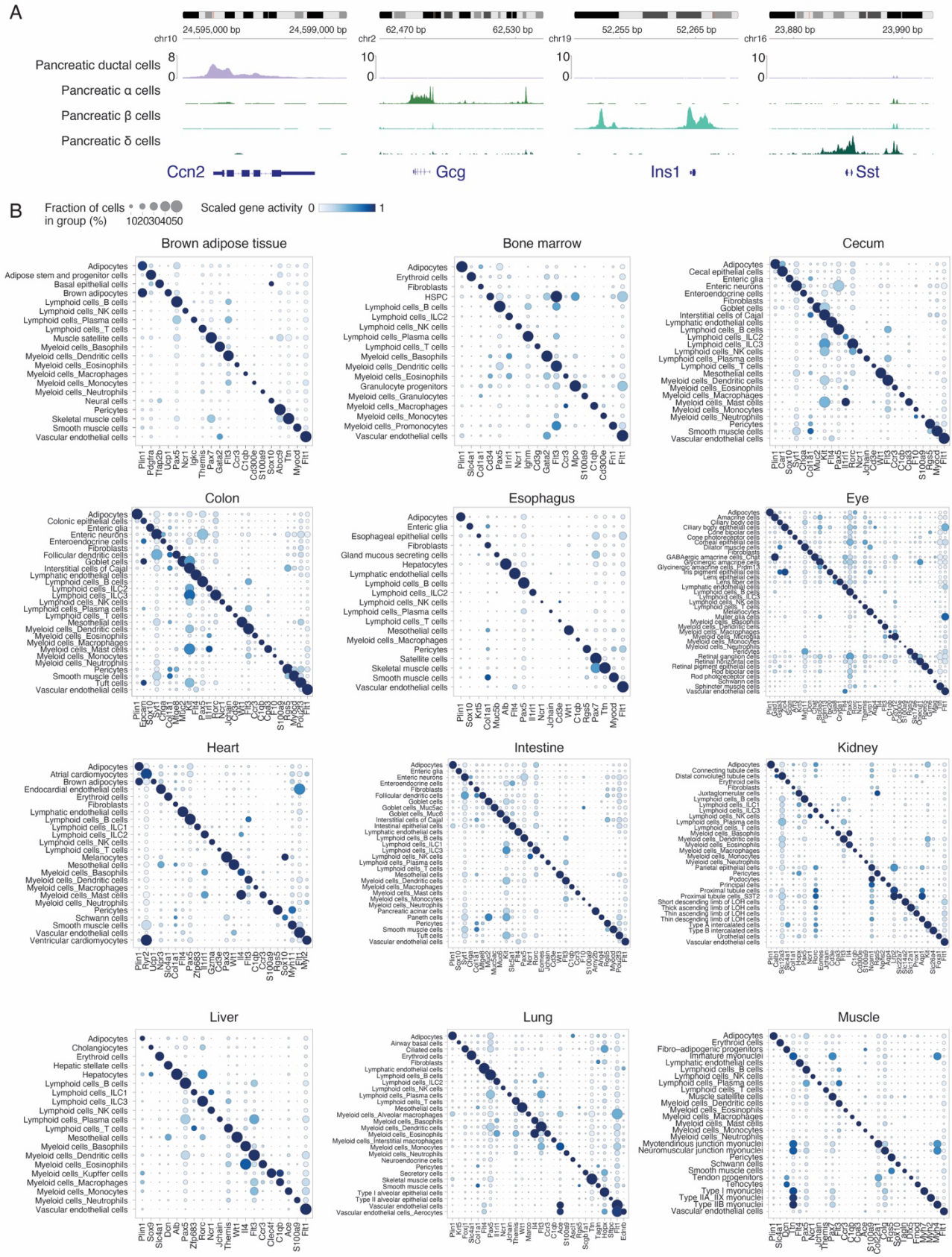

Figure S2. Annotation of main cell types using gene accessibilities.
(A) Genomic tracks showing examples of cell type annotation using accessibilities of marker genes for pancreatic ductal cells (*Ccn2*), alpha cells (*Gcg*), beta cells (*Ins1*), and delta cells (*Sst*).
(B) Dot plots showing gene markers used for annotating main cell types across tissues. The size of the dot encodes the percentage of cells within a cell type in which that marker was detected, and its color encodes the average accessibility level. A complete list of markers can be found in **Table S2**.

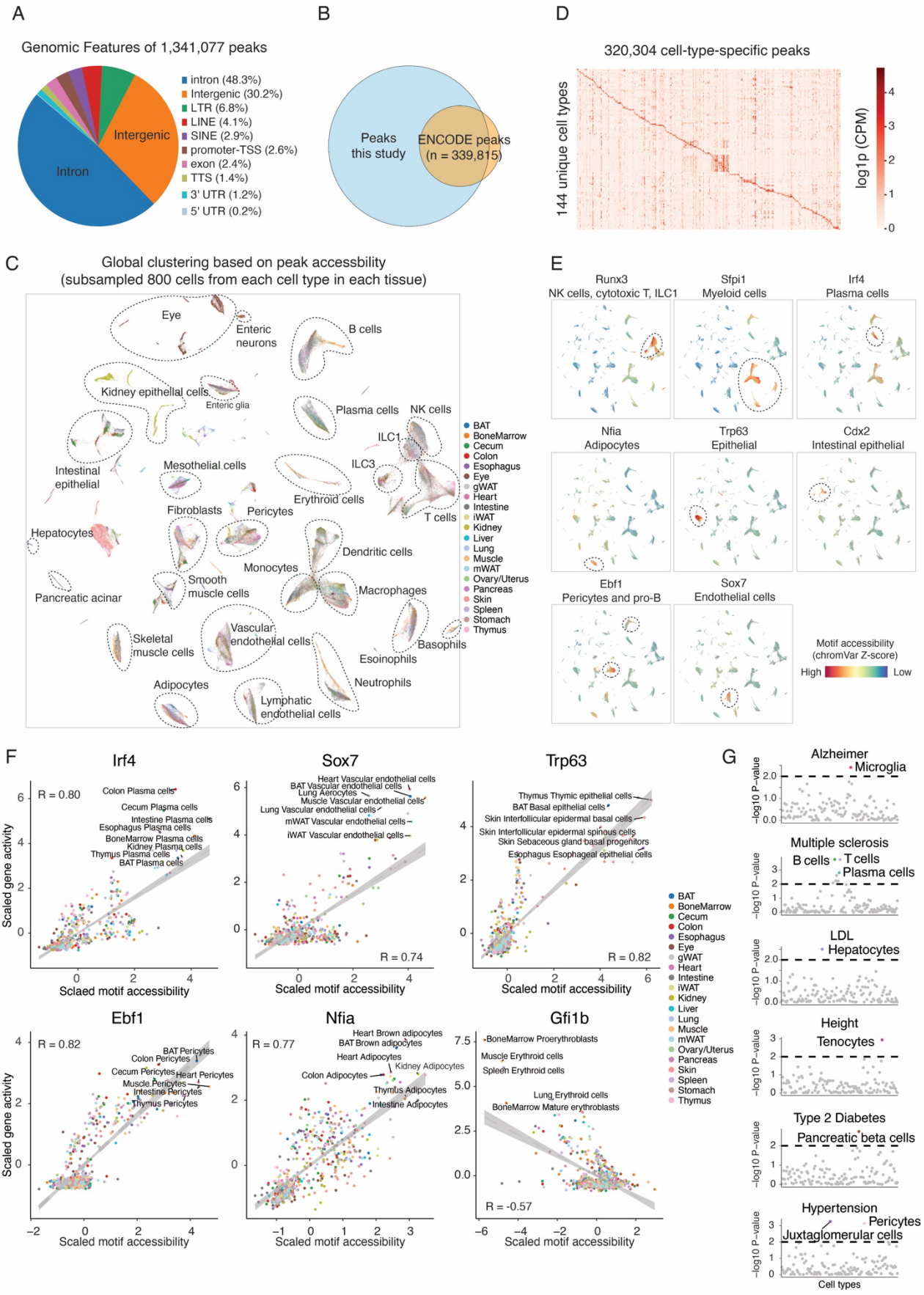

Figure S3. Identifications and characterizations of cell-type-specific cis-regulatory elements (CREs).

(A) Genomic features of 1,341,077 peaks across the mouse genome. Peaks were annotated using HOMER. TSS, transcription start site; TTS, transcription termination site; UTR, untranslated region.

(B) Venn plot showing the overlap between the peak set determined in this study and from the mouse ENCODE registry (*20*).

(C) UMAP visualization of the entire dataset subsampled to a maximum of 800 cells per main cell type per tissue, colored by the tissue type. Dimension reduction was performed using the peak-count matrix. The same cell types from multiple tissues that clustered together were circled.

(D) Heatmap showing the aggregated accessibility of peaks specific to each main cell type, quantified by counts per million.

(E) UMAP plots as in (C), colored by motif accessibilities (quantified by chromVar (*21*)) of the lineage-specific transcription factor.

(F) Scatter plots showing the example TFs whose gene accessibility levels are positively or negatively correlated with motif accessibility across cell types and tissues. Each point indicates a cell type from a specific tissue. Gene accessibilities were quantified as counts per million, and motif activities were quantified by chromVar (*21*).

(G) Scatter plots showing the enrichments of the phenotype-associated SNPs in cell-type-specific peaks. X-axis: 144 unique cell types collapsed across tissues; y-axis: significance of enrichments (-log10 p-value). Top enriched cell types were labeled for each phenotype.

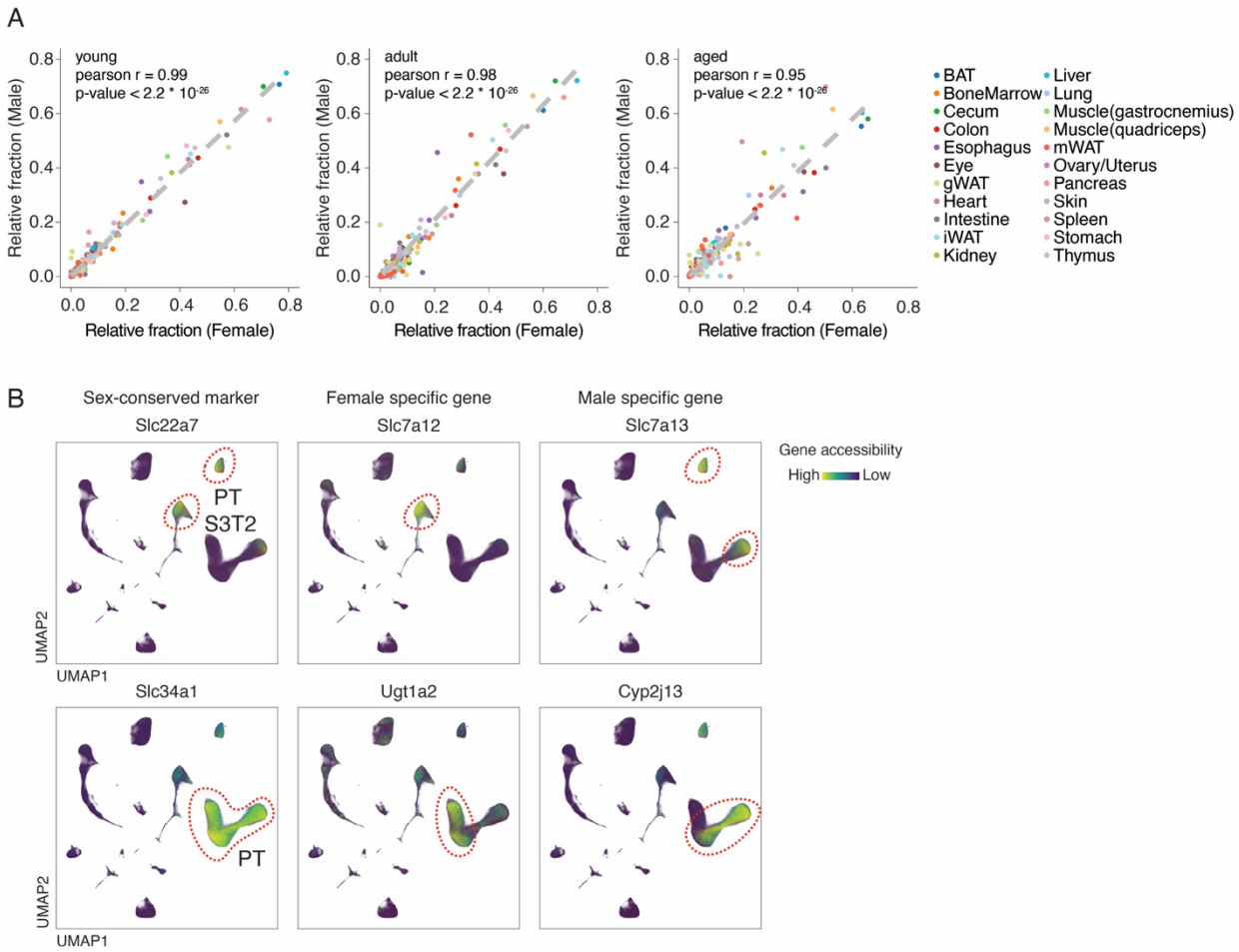

Figure S4. Examinations of sex dimorphism in cell proportion and molecular states.
(**A**) Scatterplot showing the fraction of each main cell type in each tissue between males and females, stratified by age groups. Each dot represents a cell type in a specific tissue.
(**B**) UMAP plots of all kidney cells, colored by accessibility of genes shared between sexes (left; *Slc34a1* for general proximal tubule cells (PT), *Slc22a7* for PT S3T2), unique to females (middle) and males (right).

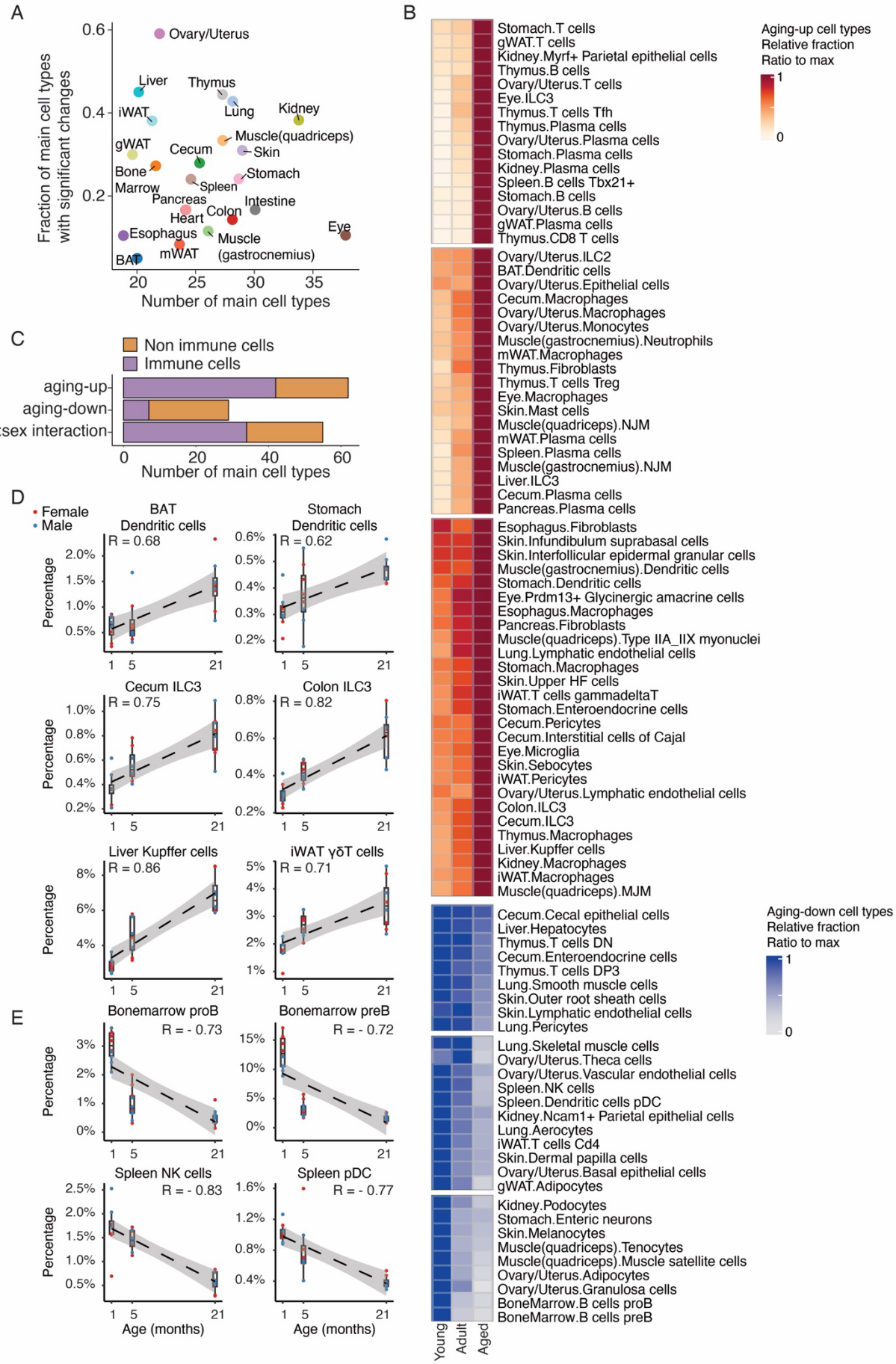

Figure S5. Aging-associated changes in main cell type proportions across tissues.
(A) Scatterplot showing the fraction of main cell types whose proportions changed significantly with age or age-sex interaction in each tissue.
(B) Heatmaps visualizing proportional changes in all aging-associated, sex-independent main cell types. The fraction of each main cell type within its tissue of origin was calculated per sample, averaged within each age group, and normalized to the most abundant condition. Cell types were ordered by hierarchical clustering implemented in ComplexHeatmap (*101*).
(C) Bar plot showing the number of main cell types derived from immune or non-immune cell types within aging-associated, sex-independent (aging-up and aging-down), or age-sex interaction groups.
(D-E) Scatter and box plots showing examples of immune cell types that expand (D) or decline (E) with age, with a linear regression line (and a Pearson correlation coefficient). Each dot represents the cell-type specific proportion of the cell type in each animal.

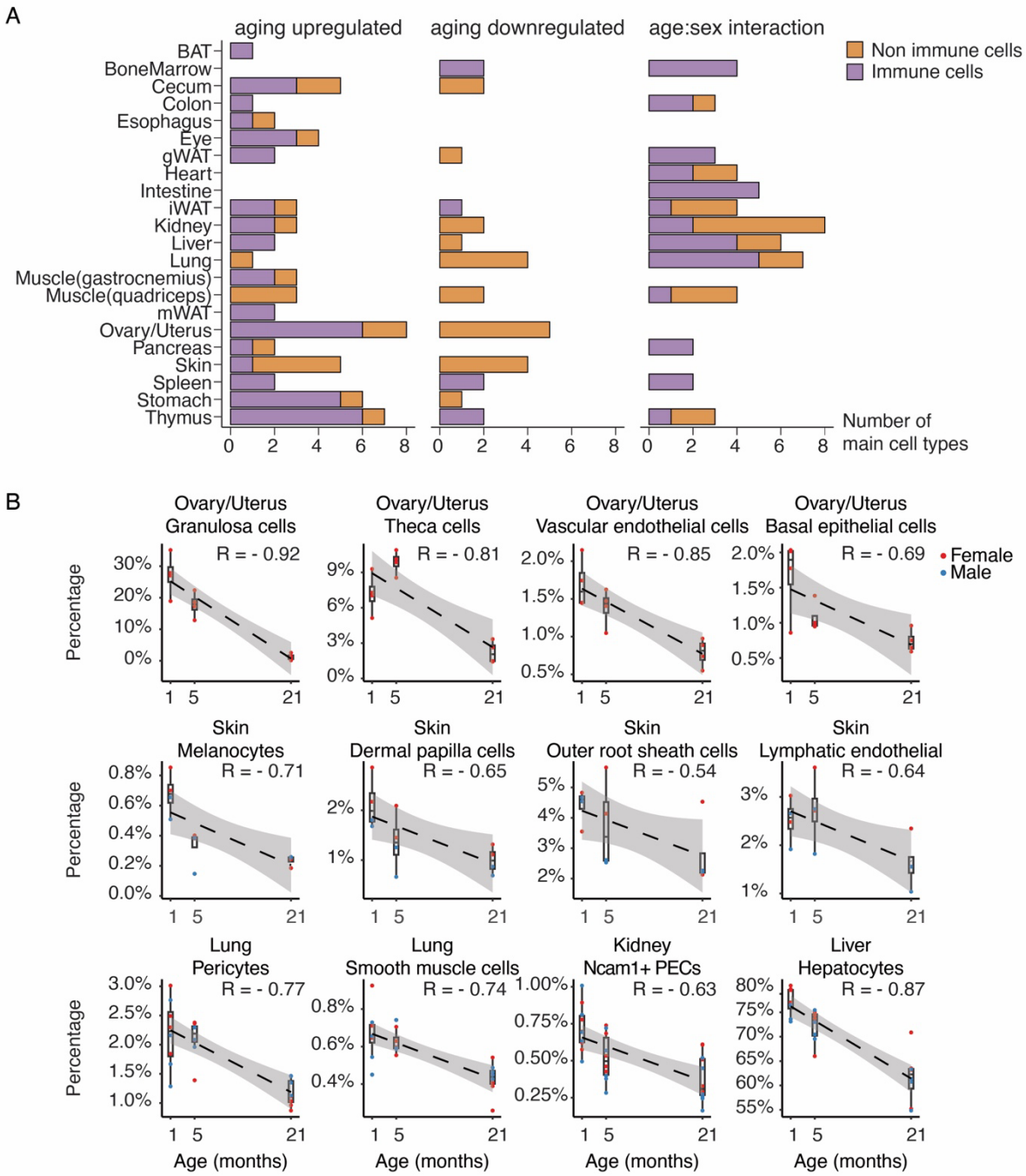

Figure S6. Aging-associated depletion of functional cell types across tissues.
(A) Bar plot showing the number of main cell types derived from immune cell types or non-immune cell types within aging-associated, sex-independent (aging-up and aging-down), or age-sex interaction groups for each tissue.
(B) Scatterplot showing examples of main cell types that decline with age across tissues, with a linear regression line (and a Pearson correlation coefficient). Each dot represents the cell-type specific proportion of the cell type in each animal.

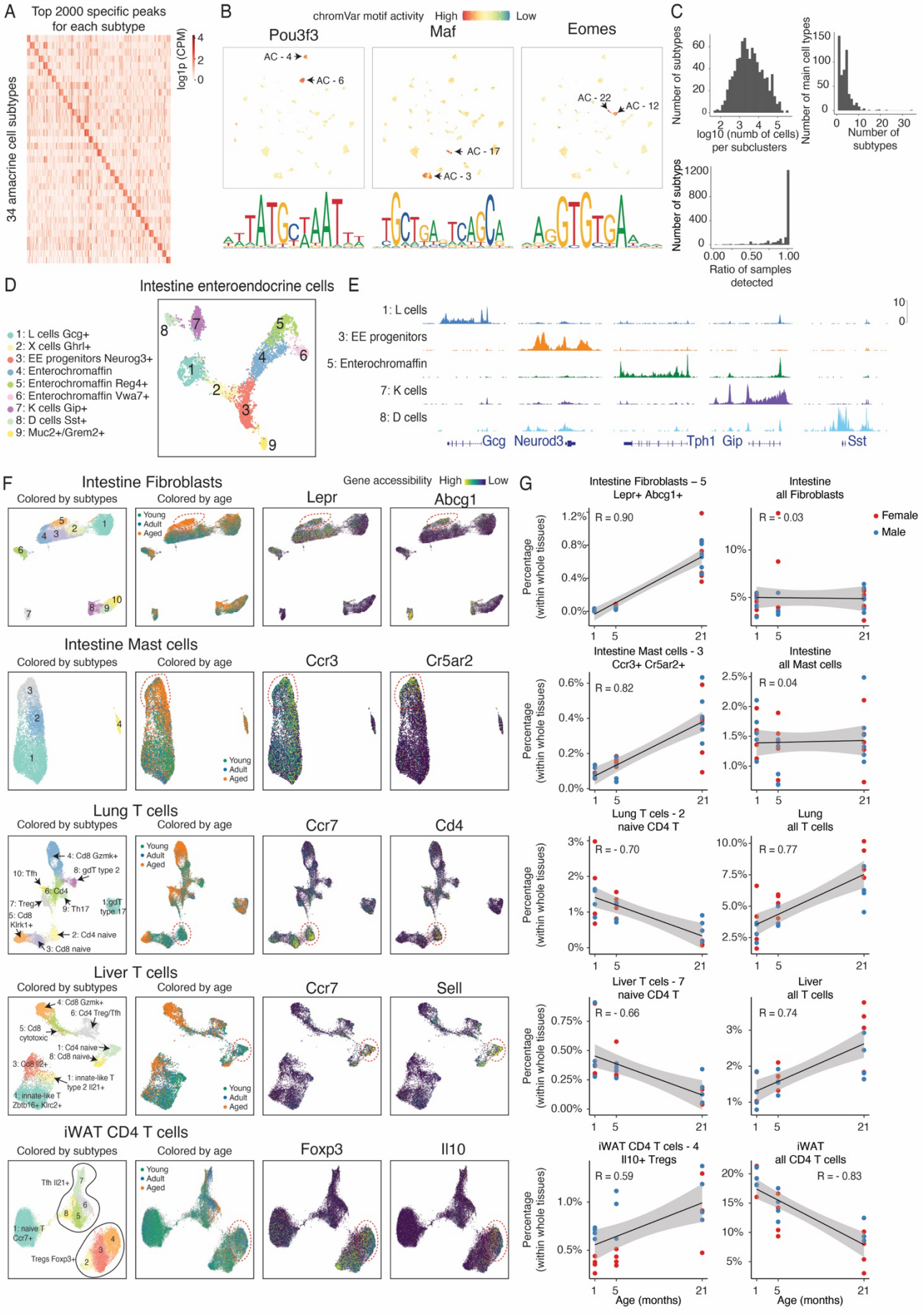

Figure S7. Identifications of cell subtypes and associated population changes in aging.

(A) Heatmap showing the aggregated accessibility of peaks specific to each main subtype in amacrine cells, quantified by counts per million.

(B) UMAP visualization of eye amacrine cells, colored by motif accessibilities of example transcription factors specific to distinct subtypes. Motif activities were quantified by chromVar (*21*).

(C) Histograms showing the distribution of cell numbers per subtype (Top left), the number of subtypes per main cell type (Top right), and the fraction of tissue samples that contain cells from each cell subtype (Bottom left).

(D) UMAP visualization of intestine enteroendocrine cells, colored by subtype identity.

(E) Genomic tracks showing the gene accessibilities marking different subtypes of intestine enteroendocrine cells.

(F) UMAP plots showing subclustering results for intestine fibroblasts, intestine mast cells, lung T cells, liver T cells and iWAT CD4 T cells, colored by subtype ID, age group, and accessibilities of genes marking circled subclusters.

(G) Scatterplot showing the proportion changes of indicated subclusters and their parental main cell types with age, along with a linear regression line.

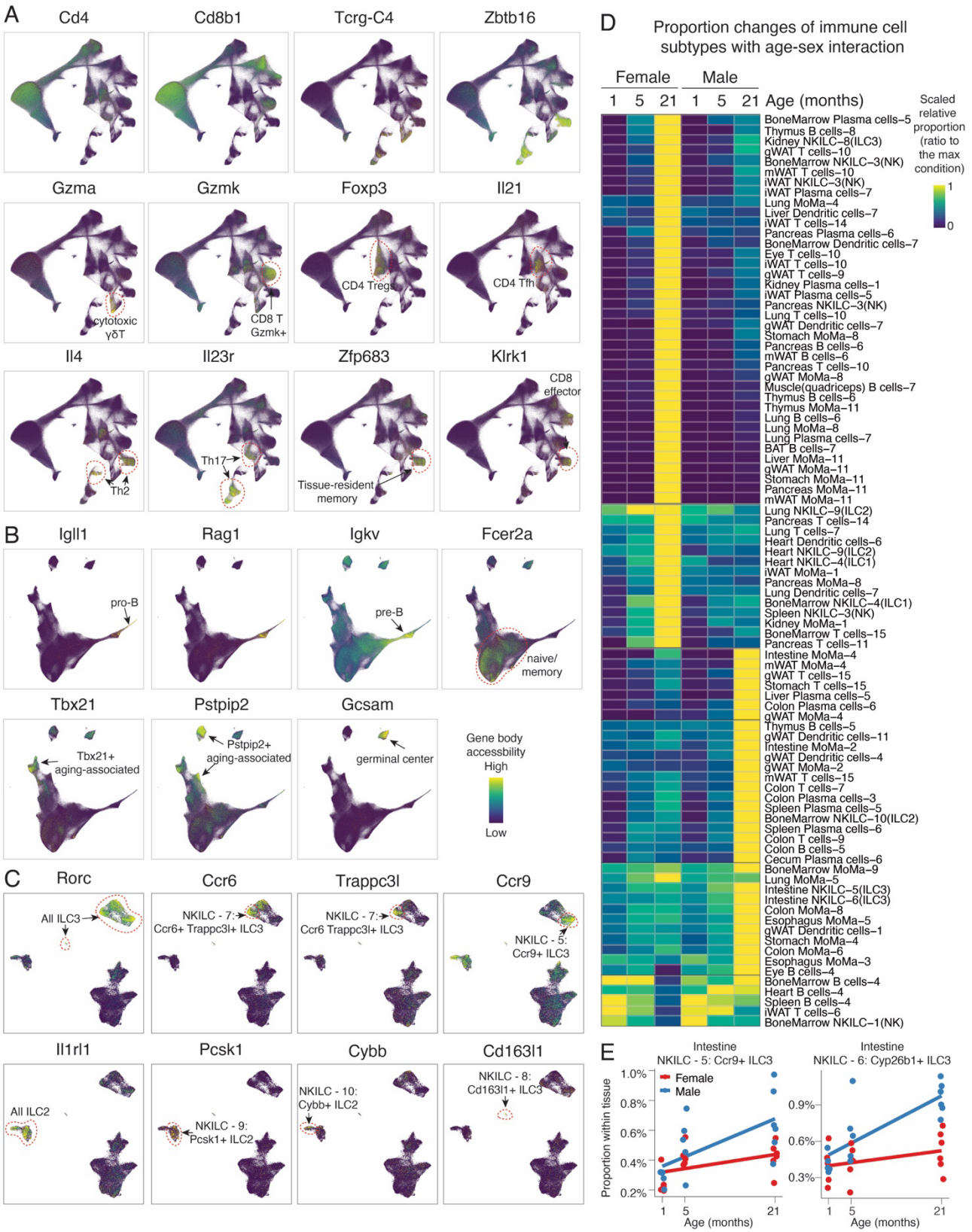

Figure S8. Global characterizations of immune cell states and their proportional changes with age.

(A) UMAP plots showing combined clustering of all T cells across tissues, colored by accessibilities of genes marking distinct subtypes.

(B) UMAP plots showing combined clustering of all B cells across tissues, colored by accessibilities of genes marking distinct subtypes.

(C) UMAP plots showing combined clustering of all innate lymphoid cells across tissues, including NK cells, ILC1, ILC2 and ILC3, colored by accessibilities of genes marking distinct subtypes.

(D) Heatmap of relative proportions of immune cell subtypes with significant age-sex interactions. Rows represent immune cell subtypes within their respective tissues, while columns correspond to mouse conditions grouped by age and sex. For each immune cell subtype within each tissue, its proportion (within each tissue) were first averaged across samples and then normalized to the maximum value within each row.

(E) Scatterplot showing male-baised expansions of *Ccr9*+ ILC3 and *Ccr6*+ *Cyp26b1*+ ILC3 in intestine along aging. Each dot represents one animal, with linear regression lines added for each sex.

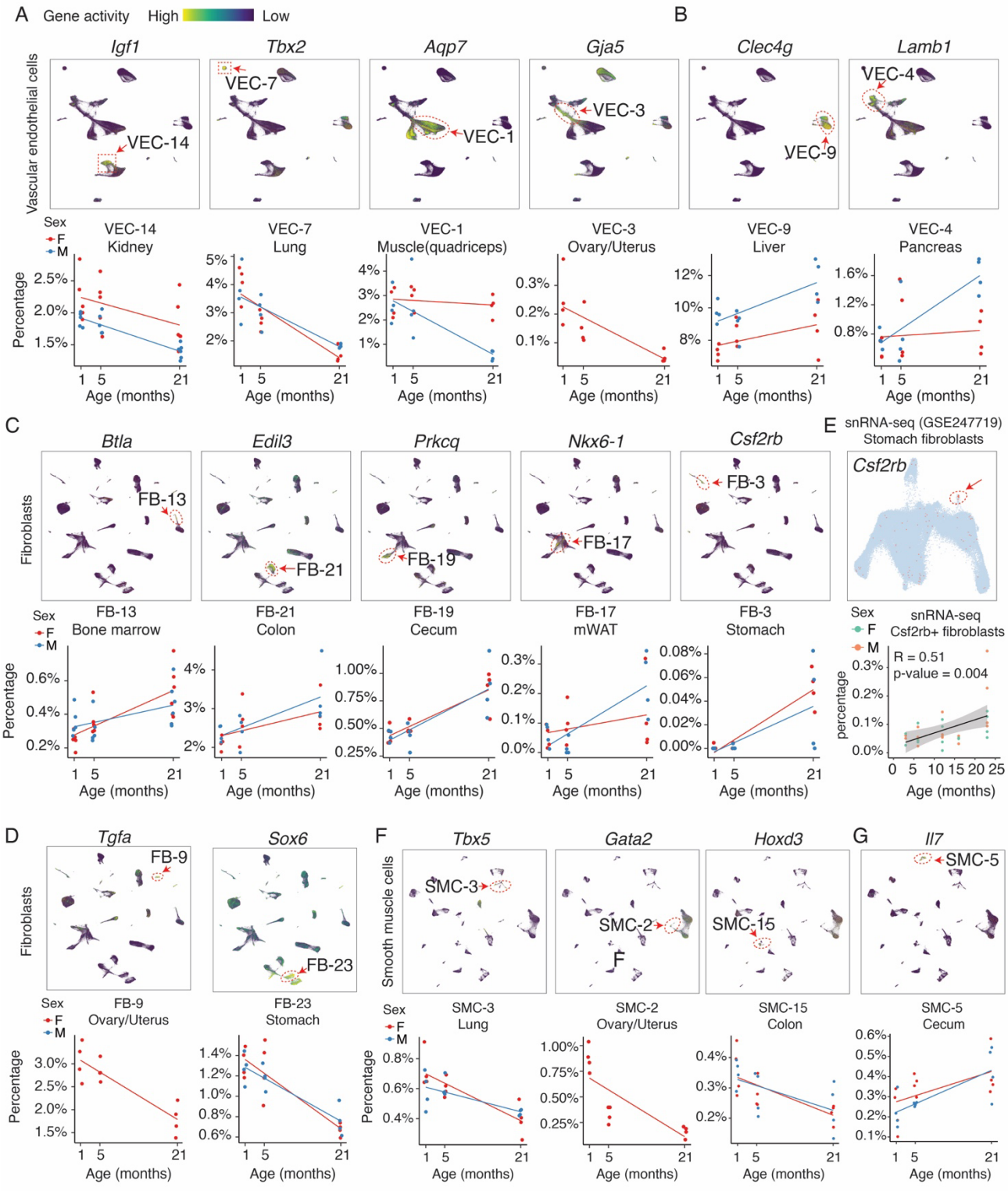

Figure S9. Cross-tissue identifications of subtypes for vascular endothelial cells, fibroblasts, smooth muscle cells and their aging-associated population changes.

(A-B) Top: UMAP plots showing the combined clustering results of vascular endothelial cells, colored by the accessibility of genes representing subtypes that expand (A) or deplete (B) with age. Bottom: Scatterplots showing the proportions of the indicated subtypes (normalized to total cells within the tissue) across three age groups, with linear regression lines added for each sex.

(C-D) UMAP plots showing the combined clustering results of fibroblasts, colored by the accessibility of genes representing subtypes that expand (C) or deplete (D) with age. Bottom: Scatterplots showing the proportions of the indicated subtypes (normalized to total cells within the tissue) across three age groups, with linear regression lines added for each sex.

(E) Validation of *Csf2rb*+ fibroblast expansion, as shown in (C), in aged stomach tissue using published snRNA-seq data (*7*). Left: UMAP plot of stomach fibroblasts colored by *Csf2rb* expression. Right: Scatterplot showing age-dependent expansion in *Csf2rb*+ fibroblasts, together with a linear regression line.

(F-G) Top: UMAP plots showing the combined clustering results of smooth muscle cells, colored by the accessibility of genes representing subtypes that deplete (F) or expand (G) with age. Bottom: Scatterplots showing the proportions of the indicated subtypes (normalized to total cells within the tissue) across three age groups, with linear regression lines added for each sex.

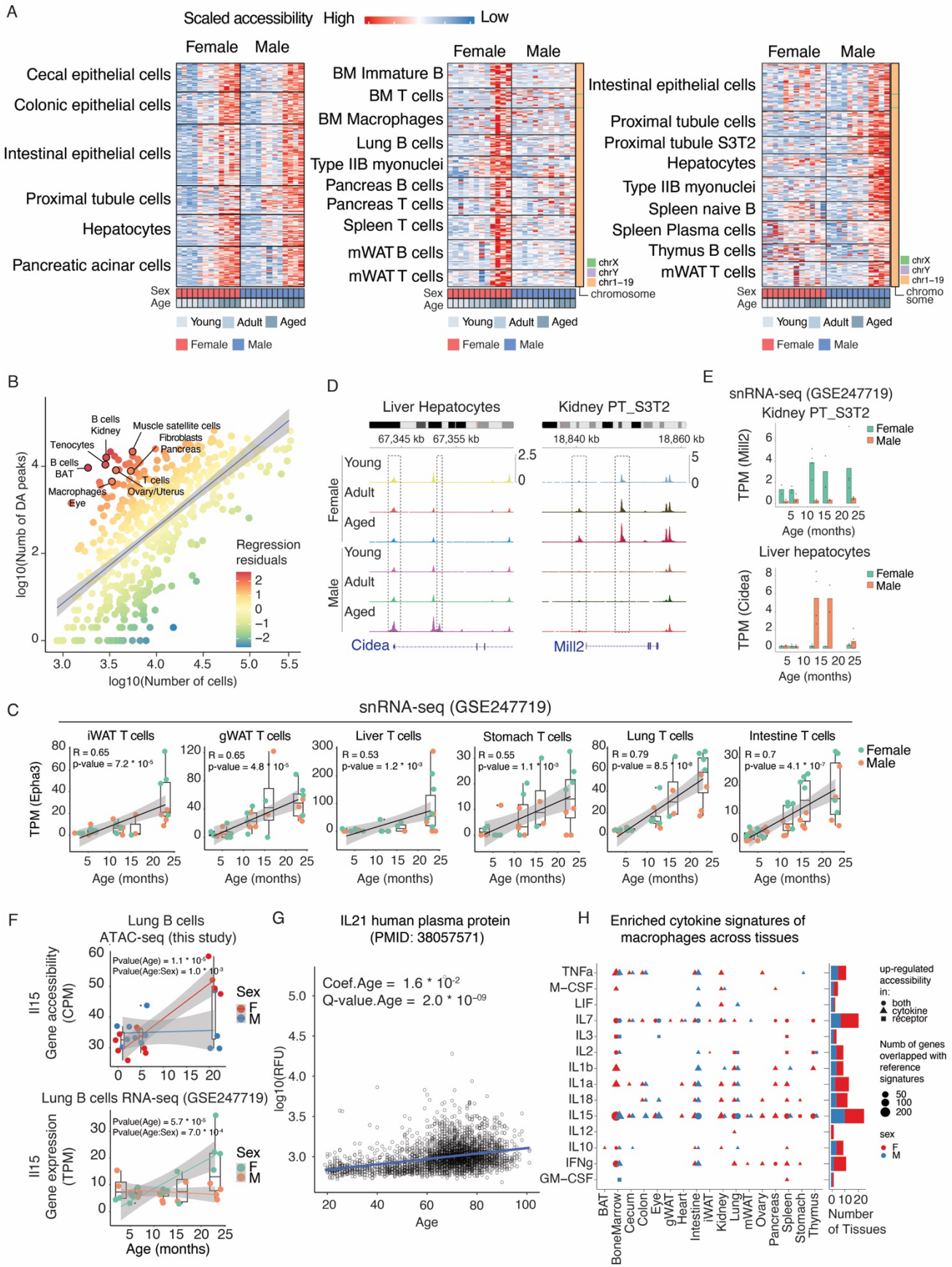

Figure S10. Identifications of cell-type-specific molecular changes in aging.
(A) Heatmaps showing examples of differentially accessible (DA) peaks that are sex-shared (left), female-specific (middle), and male-specific (right). Rows correspond to DA peaks identified in each main cell type, while columns represent individual mice. Peak accessibility was quantified as counts per million for each sample in each cell type.
(B) Scatterplot showing the correlation between the number of cells and the number of DA peaks across cell types, with a linear regression fit. Cell types with high regression residuals are labeled.
(C) Scatterplot showing the increased expression of *Epha3* in T cells across multiple tissues, with a linear regression line, validating the chromatin changes in Figure 6F.
(D) Genomic tracks of male-specific DA peak in liver hepatocytes (left) and female-specific DA peak kidney proximal tubule cells S3T2 (right).
(E) Barplot showing validation of sex-specific chromatin accessibility changes in (D) using gene expression data of the same cell type. Dot represents animals.
(F) Scatterplots showing the increased gene accessibility (top) and expression (bottom) of *Il15* in lung B cells, specifically in females, with linear regression lines added for each sex.
(G) Scatterplot showing the age-related increase in plasma protein levels of IL-21. Data was obtained from (*3*), with a linear regression line included.
(H) Left: Dot plot summarizing cytokine signatures enriched in aged macrophages across tissues. Only signatures supported by accessibility changes in secretion or receptor genes are shown. Right: Bar plot summarizing the number of tissues exhibiting activated signatures for each cytokine, separated by sex.

Supplementary Tables

Table S1. Metadata for animals included in this study.
Table S2. List of gene markers used for cell type annotations.
Table S3.List of cell-type-specific peaks, including the counts per million (CPM) value for the most accessible cell type and the mean CPM across all cell types for each peak
Table S4. Differentially abundant main cell types with age across tissues. “qvalue_age” indicates the significance of a non-zero coefficient for the age term. “qvalue_interaction” indicates the significance of a non-zero coefficient for the age-sex interaction term. “Regression R2” refers to the coefficient of determination of the regression model. “Pearson r” means the Pearson correlation r calculated between cell fraction of each main cell type within their corresponding tissues and ages, including samples of both sexes.
Table S5. Differentially abundant subtypes with age across tissues. “qvalue_age” indicates the significance of a non-zero coefficient for the age term. “qvalue_interaction” indicates the significance of a non-zero coefficient for the age-sex interaction term. “Regression R2” refers to the coefficient of determination of the regression model. “Pearson r” means the Pearson correlation r calculated between cell fraction of each subtype within their corresponding tissues and ages, including samples of both sexes.
Table S6. Differential accessible peaks with age shared in both sexes, including logFC, p-value, and q-value for each peak in both females and males.
Table S7. Differential accessible peaks with age unique to females, logFC, p-value, and q-value for each peak in both females and males.
Table S8. Differential accessible peaks with age unique to males, logFC, p-value, and q-value for each peak in both females and males.
Table S9. Aging-associated linkages with consistent changes in gene expression and chromatin accessibility at promoters and putative cis-regulatory elements. Each row represents a gene-peak-CRE linkage, including the gene name and genomic coordinates of the promoter and linked cis-regulatory site. The column “group” indicates whether the linkage is identified from both sexes or from one sex.

362 References:

363 1. T. Niccoli, L. Partridge, Ageing as a risk factor for disease. *Curr Biol* **22**, R741–52 (2012).

364 2. Y. E. Tian, V. Cropley, A. B. Maier, N. T. Lautenschlager, M. Breakspear, A. Zalesky,
365 Heterogeneous aging across multiple organ systems and prediction of chronic disease and mortality.
366 *Nat Med* **29**, 1221–1231 (2023).

367 3. H. S.-H. Oh, J. Rutledge, D. Nachun, R. Pálovics, O. Abiose, P. Moran-Losada, D. Channappa, D.
368 Y. Urey, K. Kim, Y. J. Sung, L. Wang, J. Timsina, D. Western, M. Liu, P. Kohlfeld, J. Budde, E. N.
369 Wilson, Y. Guen, T. M. Maurer, M. Haney, A. C. Yang, Z. He, M. D. Greicius, K. I. Andreasson, S.
370 Sathyan, E. F. Weiss, S. Milman, N. Barzilai, C. Cruchaga, A. D. Wagner, E. Mormino, B. Lehallier,
371 V. W. Henderson, F. M. Longo, S. B. Montgomery, T. Wyss-Coray, Organ aging signatures in the
372 plasma proteome track health and disease. *Nature* **624**, 164–172 (2023).

373 4. K. Jin, Z. Yao, C. T. J. van Velthoven, E. S. Kaplan, K. Glattfelder, S. T. Barlow, G. Boyer, D. Carey,
374 T. Casper, A. B. Chakka, R. Chakrabarty, M. Clark, M. Departee, M. Desierto, A. Gary, J. Gloe, J.
375 Goldy, N. Guilford, J. Guzman, D. Hirschstein, C. Lee, E. Liang, T. Pham, M. Reding, K.
376 Ronellenfitch, A. Ruiz, J. Sevigny, N. Shapovalova, L. Shulga, J. Sulc, A. Torkelson, H. Tung, B.
377 Levi, S. M. Sunkin, N. Dee, L. Esposito, K. A. Smith, B. Tasic, H. Zeng, Brain-wide cell-type-specific
378 transcriptomic signatures of healthy ageing in mice. *Nature*, doi: 10.1038/s41586-024-08350-8
379 (2025).

380 5. R. Wang, P. Zhang, J. Wang, L. Ma, W. E, S. Suo, M. Jiang, J. Li, H. Chen, H. Sun, L. Fei, Z. Zhou,
381 Y. Zhou, Y. Chen, W. Zhang, X. Wang, Y. Mei, Z. Sun, C. Yu, J. Shao, Y. Fu, Y. Xiao, F. Ye, X.
382 Fang, H. Wu, Q. Guo, X. Fang, X. Li, X. Gao, D. Wang, P.-F. Xu, R. Zeng, G. Xu, L. Zhu, L. Wang,
383 J. Qu, D. Zhang, H. Ouyang, H. Huang, M. Chen, S.-C. Ng, G.-H. Liu, G.-C. Yuan, G. Guo, X. Han,
384 Construction of a cross-species cell landscape at single-cell level. *Nucleic Acids Res* **51**, 501–516
385 (2023).

386 6. T.-C. Lu, M. Brbić, Y.-J. Park, T. Jackson, J. Chen, S. S. Kolluru, Y. Qi, N. S. Katheder, X. T. Cai, S.
387 Lee, Y.-C. Chen, N. Auld, C.-Y. Liang, S. H. Ding, D. Welsch, S. D'Souza, A. O. Pisco, R. C. Jones,
388 J. Leskovec, E. C. Lai, H. J. Bellen, L. Luo, H. Jasper, S. R. Quake, H. Li, Aging Fly Cell Atlas
389 identifies exhaustive aging features at cellular resolution. *Science* **380**, eadg0934 (2023).

390 7. Z. Zhang, C. Schaefer, W. Jiang, Z. Lu, J. Lee, A. Sziraki, A. Abdulraouf, B. Wick, M. Haeussler, Z.
391 Li, G. Molla, R. Satija, W. Zhou, J. Cao, A panoramic view of cell population dynamics in mammalian
392 aging. *Science* **387**, eadn3949 (2025).

393 8. J. J. Beintema, R. N. Campagne, M. Gruber, Rat pancreatic ribonuclease. I. Isolation and properties.
394 *Biochim Biophys Acta* **310**, 148–160 (1973).

395 9. A. M. Al-Adsani, S. A. Barhoush, N. K. Bastaki, S. A. Al-Bustan, K. K. Al-Qattan, Comparing and
396 Optimizing RNA Extraction from the Pancreas of Diabetic and Healthy Rats for Gene Expression
397 Analyses. *Genes (Basel)* **13** (2022).

398 10. F. V. De Rop, G. Hulselmans, C. Flerin, P. Soler-Vila, A. Rafels, V. Christiaens, C. B. González-
399 Blas, D. Marchese, G. Caratù, S. Poovathingal, O. Rozenblatt-Rosen, M. Slyper, W. Luo, C. Muus,
400 F. Duarte, R. Shrestha, S. T. Bagdatli, M. R. Corces, L. Mamanova, A. Knights, K. B. Meyer, R.
401 Mulqueen, A. Taherinasab, P. Maschmeyer, J. Pezoldt, C. L. G. Lambert, M. Iglesias, S. R. Najle, Z.
402 Y. Dossani, L. G. Martelotto, Z. Burkett, R. Lebofsky, J. I. Martin-Subero, S. Pillai, A. Sebé-Pedrós,
403 B. Deplancke, S. A. Teichmann, L. S. Ludwig, T. P. Braun, A. C. Adey, W. J. Greenleaf, J. D.
404 Buenrostro, A. Regev, S. Aerts, H. Heyn, Systematic benchmarking of single-cell ATAC-sequencing
405 protocols. *Nat Biotechnol* **42**, 916–926 (2024).

11. S. Domcke, A. J. Hill, R. M. Daza, J. Cao, D. R. O'Day, H. A. Pliner, K. A. Aldinger, D. Pokholok, F. Zhang, J. H. Milbank, M. A. Zager, I. A. Glass, F. J. Steemers, D. Doherty, C. Trapnell, D. A. Cusanovich, J. Shendure, A human cell atlas of fetal chromatin accessibility. *Science* **370** (2020).

12. K. Zhang, J. D. Hocker, M. Miller, X. Hou, J. Chiou, O. B. Poirion, Y. Qiu, Y. E. Li, K. J. Gaulton, A. Wang, S. Preissl, B. Ren, A single-cell atlas of chromatin accessibility in the human genome. *Cell* **184**, 5985–6001.e19 (2021).

13. Y. E. Li, S. Preissl, M. Miller, N. D. Johnson, Z. Wang, H. Jiao, C. Zhu, Z. Wang, Y. Xie, O. Poirion, C. Kern, A. Pinto-Duarte, W. Tian, K. Siletti, N. Emerson, J. Osteen, J. Lucero, L. Lin, Q. Yang, Q. Zhu, N. Zemke, S. Espinoza, A. M. Yanny, J. Nyhus, N. Dee, T. Casper, N. Shapovalova, D. Hirschstein, R. D. Hodge, S. Linnarsson, T. Bakken, B. Levi, C. D. Keene, J. Shang, E. Lein, A. Wang, M. M. Behrens, J. R. Ecker, B. Ren, A comparative atlas of single-cell chromatin accessibility in the human brain. *Science* **382**, eadf7044 (2023).

14. S. Zu, Y. E. Li, K. Wang, E. J. Armand, S. Mamde, M. L. Amaral, Y. Wang, A. Chu, Y. Xie, M. Miller, J. Xu, Z. Wang, K. Zhang, B. Jia, X. Hou, L. Lin, Q. Yang, S. Lee, B. Li, S. Kuan, H. Liu, J. Zhou, A. Pinto-Duarte, J. Lucero, J. Osteen, M. Nunn, K. A. Smith, B. Tasic, Z. Yao, H. Zeng, Z. Wang, J. Shang, M. M. Behrens, J. R. Ecker, A. Wang, S. Preissl, B. Ren, Single-cell analysis of chromatin accessibility in the adult mouse brain. *Nature* **624**, 378–389 (2023).

15. A. Sziraki, Z. Lu, J. Lee, G. Banyai, S. Anderson, A. Abdulraouf, E. Metzner, A. Liao, J. Banfelder, A. Epstein, C. Schaefer, Z. Xu, Z. Zhang, L. Gan, P. T. Nelson, W. Zhou, J. Cao, A global view of aging and Alzheimer's pathogenesis-associated cell population dynamics and molecular signatures in human and mouse brains. *Nature Genetics* **55**, 2104–2116 (2023).

16. Z. Lu, M. Zhang, J. Lee, A. Sziraki, S. Anderson, Z. Zhang, Z. Xu, W. Jiang, S. Ge, P. T. Nelson, W. Zhou, J. Cao, Tracking cell-type-specific temporal dynamics in human and mouse brains. *Cell* **186**, 4345–4364.e24 (2023).

17. K. Zhang, N. R. Zemke, E. J. Armand, B. Ren, A fast, scalable and versatile tool for analysis of single-cell omics data. *Nature Methods* **21**, 217–227 (2024).

18. A. Charrier, D. R. Brigstock, Regulation of pancreatic function by connective tissue growth factor (CTGF, CCN2). *Cytokine Growth Factor Rev* **24**, 59–68 (2013).

19. Å. Segerstolpe, A. Palasantza, P. Eliasson, E.-M. Andersson, A.-C. Andréasson, X. Sun, S. Picelli, A. Sabirsh, M. Clausen, M. K. Bjursell, D. M. Smith, M. Kasper, C. Ämmälä, R. Sandberg, Single-Cell Transcriptome Profiling of Human Pancreatic Islets in Health and Type 2 Diabetes. *Cell Metab* **24**, 593–607 (2016).

20. J. E. Moore, M. J. Purcaro, H. E. Pratt, C. B. Epstein, N. Shoresh, J. Adrian, T. Kawli, C. A. Davis, A. Dobin, R. Kaul, J. Halow, E. L. Van Nostrand, P. Freese, D. U. Gorkin, Y. Shen, Y. He, M. Mackiewicz, F. Pauli-Behn, B. A. Williams, A. Mortazavi, C. A. Keller, X.-O. Zhang, S. I. Elhajjajy, J. Huey, D. E. Dickel, V. Snetkova, X. Wei, X. Wang, J. C. Rivera-Mulia, J. Rozowsky, J. Zhang, S. B. Chhetri, J. Zhang, A. Victorsen, K. P. White, A. Visel, G. W. Yeo, C. B. Burge, E. Lécuyer, D. M. Gilbert, J. Dekker, J. Rinn, E. M. Mendenhall, J. R. Ecker, M. Kellis, R. J. Klein, W. S. Noble, A. Kundaje, R. Guigó, P. J. Farnham, J. M. Cherry, R. M. Myers, B. Ren, B. R. Graveley, M. B. Gerstein, L. A. Pennacchio, M. P. Snyder, B. E. Bernstein, B. Wold, R. C. Hardison, T. R. Gingeras, J. A. Stamatoyannopoulos, Z. Weng, Expanded encyclopaedias of DNA elements in the human and mouse genomes. *Nature* **583**, 699–710 (2020).

21. A. N. Schep, B. Wu, J. D. Buenrostro, W. J. Greenleaf, chromVAR: inferring transcription-factor-associated accessibility from single-cell epigenomic data. *Nat. Methods* **14**, 975–978 (2017).

22. Q. Shan, Z. Zeng, S. Xing, F. Li, S. M. Hartwig, J. A. Gullicksrud, S. P. Kurup, N. Van Braeckel-

Budimir, Y. Su, M. D. Martin, S. M. Varga, I. Taniuchi, J. T. Harty, W. Peng, V. P. Badovinac, H.-H. Xue, The transcription factor Runx3 guards cytotoxic CD8 effector T cells against deviation towards follicular helper T cell lineage. *Nat Immunol* **18**, 931–939 (2017).

23. C. V. Laiosa, M. Stadtfeld, T. Graf, Determinants of lymphoid-myeloid lineage diversification. *Annu Rev Immunol* **24**, 705–738 (2006).

24. U. Klein, S. Casola, G. Cattoretti, Q. Shen, M. Lia, T. Mo, T. Ludwig, K. Rajewsky, R. Dalla-Favera, Transcription factor IRF4 controls plasma cell differentiation and class-switch recombination. *Nat Immunol* **7**, 773–782 (2006).

25. R. Nechanitzky, D. Akbas, S. Scherer, I. Györy, T. Hoyler, S. Ramamoorthy, A. Diefenbach, R. Grosschedl, Transcription factor EBF1 is essential for the maintenance of B cell identity and prevention of alternative fates in committed cells. *Nature Immunology* **14**, 867–875 (2013).

26. F. Pagani, E. Tratta, P. Dell'Era, M. Cominelli, P. L. Poliani, EBF1 is expressed in pericytes and contributes to pericyte cell commitment. *Histochem Cell Biol* **156**, 333–347 (2021).

27. D. McClellan, M. J. Casey, D. Bareyan, H. Lucente, C. Ours, M. Velinder, J. Singer, M. D. Lone, W. Sun, Y. Coria, C. C. Mason, M. E. Engel, Growth Factor Independence 1B-Mediated Transcriptional Repression and Lineage Allocation Require Lysine-Specific Demethylase 1-Dependent Recruitment of the BHC Complex. *Mol Cell Biol* **39** (2019).

28. B. K. Bulik-Sullivan, P.-R. Loh, H. K. Finucane, S. Ripke, J. Yang, N. Patterson, M. J. Daly, A. L. Price, B. M. Neale, LD Score regression distinguishes confounding from polygenicity in genome-wide association studies. *Nature Genetics* **47**, 291–295 (2015).

29. Y. Li, S. M. Laws, L. A. Miles, J. S. Wiley, X. Huang, C. L. Masters, B. J. Gu, Genomics of Alzheimer's disease implicates the innate and adaptive immune systems. *Cell Mol Life Sci* **78**, 7397–7426 (2021).

30. C. Scholz, K. T. Patton, D. E. Anderson, G. J. Freeman, D. A. Hafler, Expansion of autoreactive T cells in multiple sclerosis is independent of exogenous B7 costimulation. *J Immunol* **160**, 1532–1538 (1998).

31. G. Comi, A. Bar-Or, H. Lassmann, A. Uccelli, H.-P. Hartung, X. Montalban, P. S. Sørensen, R. Hohlfeld, S. L. Hauser, Expert Panel of the 27th Annual Meeting of the European Charcot Foundation, Role of B Cells in Multiple Sclerosis and Related Disorders. *Ann Neurol* **89**, 13–23 (2021).

32. J. L. Goldstein, M. S. Brown, Regulation of low-density lipoprotein receptors: implications for pathogenesis and therapy of hypercholesterolemia and atherosclerosis. *Circulation* **76**, 504–507 (1987).

33. C. Wysham, J. Shubrook, Beta-cell failure in type 2 diabetes: mechanisms, markers, and clinical implications. *Postgrad Med* **132**, 676–686 (2020).

34. H. Yamaguchi, R. A. Gomez, M. L. S. Sequeira-Lopez, Renin Cells, From Vascular Development to Blood Pressure Sensing. *Hypertension* **80**, 1580–1589 (2023).

35. L. Rodríguez-Montes, S. Ovchinnikova, X. Yuan, T. Studer, I. Sarropoulos, S. Anders, H. Kaessmann, M. Cardoso-Moreira, Sex-biased gene expression across mammalian organ development and evolution. *Science*, doi: 10.1126/science.adf1046 (2023).

36. A. Christianto, T. Baba, F. Takahashi, K. Inui, M. Inoue, M. Suyama, Y. Ono, Y. Ohkawa, K.-I. Morohashi, Sex differences in metabolic pathways are regulated by Pfkfb3 and Pdk4 expression in

rodent muscle. *Commun Biol* **4**, 1264 (2021).

37. D. Janosevic, J. Myslinski, T. W. McCarthy, A. Zollman, F. Syed, X. Xuei, H. Gao, Y.-L. Liu, K. S. Collins, Y.-H. Cheng, S. Winfree, T. M. El-Achkar, B. Maier, R. Melo Ferreira, M. T. Eadon, T. Hato, P. C. Dagher, The orchestrated cellular and molecular responses of the kidney to endotoxin define a precise sepsis timeline. *Elife* **10** (2021).

38. A. Jagger, Y. Shimojima, J. J. Goronzy, C. M. Weyand, Regulatory T cells and the immune aging process: a mini-review. *Gerontology* **60**, 130–137 (2014).

39. X. Li, C. Li, W. Zhang, Y. Wang, P. Qian, H. Huang, Inflammation and aging: signaling pathways and intervention therapies. *Signal Transduct Target Ther* **8**, 239 (2023).

40. D. Frasca, M. Romero, D. Garcia, A. Diaz, B. B. Blomberg, Hyper-metabolic B cells in the spleens of old mice make antibodies with autoimmune specificities. *Immun Ageing* **18**, 9 (2021).

41. S. N. Hilmer, V. C. Cogger, D. G. Le Couteur, Basal activity of Kupffer cells increases with old age. *J Gerontol A Biol Sci Med Sci* **62**, 973–978 (2007).

42. S. Mukherjee, M. E. C. Bruno, J. Oakes, G. S. Hawk, A. J. Stromberg, D. A. Cohen, M. E. Starr, Mechanisms of γδ T cell accumulation in visceral adipose tissue with aging. *Front Aging* **4**, 1258836 (2023).

43. Systematic analysis of muscle aging using joint single-cell and single-nucleus sequencing. *Nat Aging* **4**, 621–622 (2024).

44. F. M. Gribble, F. Reimann, Function and mechanisms of enteroendocrine cells and gut hormones in metabolism. *Nat Rev Endocrinol* **15**, 226–237 (2019).

45. J. de Mol, J. Kuiper, D. Tsiantoulas, A. C. Foks, The Dynamics of B Cell Aging in Health and Disease. *Front Immunol* **12**, 733566 (2021).

46. R. Aspinall, Age-associated thymic atrophy in the mouse is due to a deficiency affecting rearrangement of the TCR during intrathymic T cell development. *J Immunol* **158**, 3037–3045 (1997).

47. K. B. Menees, R. H. Earls, J. Chung, J. Jernigan, N. M. Filipov, J. M. Carpenter, J.-K. Lee, Sex- and age-dependent alterations of splenic immune cell profile and NK cell phenotypes and function in C57BL/6J mice. *Immun Ageing* **18**, 3 (2021).

48. E. R. Zacca, M. I. Crespo, R. P. Acland, E. Roselli, N. G. Núñez, M. Maccioni, B. A. Maletto, M. C. Pistoresi-Palencia, G. Morón, Aging Impairs the Ability of Conventional Dendritic Cells to Cross-Prime CD8+ T Cells upon Stimulation with a TLR7 Ligand. *PLoS One* **10**, e0140672 (2015).

49. C. Jin, X. Wang, J. Yang, S. Kim, A. D. Hudgins, A. Gamliel, M. Pei, D. Contreras, M. Devos, Q. Guo, J. Vijg, M. Conti, J. Hoeijmakers, J. Campisi, R. Lobo, Z. Williams, M. G. Rosenfeld, Y. Suh, Molecular and genetic insights into human ovarian aging from single-nuclei multi-omics analyses. *Nat Aging*, doi: 10.1038/s43587-024-00762-5 (2024).

50. F. J. Broekmans, M. R. Soules, B. C. Fauser, Ovarian aging: mechanisms and clinical consequences. *Endocr Rev* **30**, 465–493 (2009).

51. J. P. Ortonne, Pigmentary changes of the ageing skin. *Br J Dermatol* **122 Suppl 35**, 21–28 (1990).

52. R. P. Kataru, H. J. Park, J. Shin, J. E. Baik, A. Sarker, S. Brown, B. J. Mehrara, Structural and Functional Changes in Aged Skin Lymphatic Vessels. *Front Aging* **3**, 864860 (2022).

53. A. Gillich, F. Zhang, C. G. Farmer, K. J. Travaglini, S. Y. Tan, M. Gu, B. Zhou, J. A. Feinstein, M. A. Krasnow, R. J. Metzger, Capillary cell-type specialization in the alveolus. *Nature* **586**, 785–789 (2020).

54. E. A. Hermann, A. Motahari, E. A. Hoffman, N. Allen, A. G. Bertoni, D. A. Bluemke, A. Eskandari, S. E. Gerard, J. Guo, G. T. Hiura, D. W. Kaczka, E. D. Michos, P. Nagpal, J. Pankow, S. Shah, B. M. Smith, K. Hinckley Stukovsky, Y. Sun, K. Watson, R. G. Barr, Pulmonary Blood Volume Among Older Adults in the Community: The MESA Lung Study. *Circ Cardiovasc Imaging* **15**, e014380 (2022).

55. S. J. Shankland, Y. Wang, A. S. Shaw, J. C. Vaughan, J. W. Pippin, O. Wessely, Podocyte Aging: Why and How Getting Old Matters. *J Am Soc Nephrol* **32**, 2697–2713 (2021).

56. W.-B. Liu, G.-R. Huang, B.-L. Liu, H.-K. Hu, J. Geng, H.-L. Rui, C. Gao, Y.-J. Huang, G.-Y. Huo, J.-R. Mao, C.-J. Lu, A.-L. Xu, Single cell landscape of parietal epithelial cells in healthy and diseased states. *Kidney Int* **104**, 108–123 (2023).

57. Tabula Muris Consortium, A single-cell transcriptomic atlas characterizes ageing tissues in the mouse. *Nature* **583**, 590–595 (2020).

58. W.-C. Tsai, H.-N. Chang, T.-Y. Yu, C.-H. Chien, L.-F. Fu, F.-C. Liang, J.-H. S. Pang, Decreased proliferation of aging tenocytes is associated with down-regulation of cellular senescence-inhibited gene and up-regulation of p27. *J Orthop Res* **29**, 1598–1603 (2011).

59. J. V. Chakkalakal, K. M. Jones, M. A. Basson, A. S. Brack, The aged niche disrupts muscle stem cell quiescence. *Nature* **490**, 355–360 (2012).

60. R. Pellegrino, R. Paganelli, A. Di Iorio, S. Bandinelli, A. Moretti, G. Iolascon, E. Sparvieri, D. Tarantino, L. Ferrucci, Temporal trends, sex differences, and age-related disease influence in Neutrophil, Lymphocyte count and Neutrophil to Lymphocyte-ratio: results from InCHIANTI follow-up study. *Immun Ageing* **20**, 46 (2023).

61. P. J. Busse, S. K. Mathur, Age-related changes in immune function: effect on airway inflammation. *J Allergy Clin Immunol* **126**, 690–9; quiz 700–1 (2010).

62. J. Li, J. Choi, X. Cheng, J. Ma, S. Pema, J. R. Sanes, G. Mardon, B. J. Frankfort, N. M. Tran, Y. Li, R. Chen, Comprehensive single-cell atlas of the mouse retina. *iScience* **27**, 109916 (2024).

63. S. J. Purohit, R. P. Stephan, H.-G. Kim, B. R. Herrin, L. Gartland, C. A. Klug, Determination of lymphoid cell fate is dependent on the expression status of the IL-7 receptor. *EMBO J* **22**, 5511–5521 (2003).

64. D. M. Poscablo, A. K. Worthington, S. Smith-Berdan, M. G. E. Rommel, B. A. Manso, R. Adili, L. Mok, R. E. Reggiardo, T. Cool, R. Mogharrab, J. Myers, S. Dahmen, P. Medina, A. E. Beaudin, S. W. Boyer, M. Holinstat, V. D. Jonsson, E. C. Forsberg, An age-progressive platelet differentiation path from hematopoietic stem cells causes exacerbated thrombosis. *Cell* **187**, 3090–3107.e21 (2024).

65. S. J. Dumas, E. Meta, M. Borri, J. Goveia, K. Rohlenova, N. V. Conchinha, K. Falkenberg, L.-A. Teuwen, L. de Rooij, J. Kalucka, R. Chen, S. Khan, F. Taverna, W. Lu, M. Parys, C. De Legher, S. Vinckier, T. K. Karakach, L. Schoonjans, L. Lin, L. Bolund, M. Dewerchin, G. Eelen, T. J. Rabelink, X. Li, Y. Luo, P. Carmeliet, Single-Cell RNA Sequencing Reveals Renal Endothelium Heterogeneity and Metabolic Adaptation to Water Deprivation. *J Am Soc Nephrol* **31**, 118–138 (2020).

66. D. A. Mogilenko, I. Shchukina, M. N. Artyomov, Immune ageing at single-cell resolution. *Nature Reviews Immunology* **22**, 484–498 (2021).

67. M. Kohyama, W. Ise, B. T. Edelson, P. R. Wilker, K. Hildner, C. Mejia, W. A. Frazier, T. L. Murphy, K. M. Murphy, Role for Spi-C in the development of red pulp macrophages and splenic iron homeostasis. *Nature* **457**, 318–321 (2009).

68. T. A. Fehniger, S. F. Cai, X. Cao, A. J. Bredemeyer, R. M. Presti, A. R. French, T. J. Ley, Acquisition of murine NK cell cytotoxicity requires the translation of a pre-existing pool of granzyme B and perforin mRNAs. *Immunity* **26**, 798–811 (2007).

69. V. Chiurchiù, M. Lanuti, M. De Bardi, L. Battistini, M. Maccarrone, The differential characterization of GPR55 receptor in human peripheral blood reveals a distinctive expression in monocytes and NK cells and a proinflammatory role in these innate cells. *Int Immunol* **27**, 153–160 (2015).

70. Gender differences in autoimmune disease. *Frontiers in Neuroendocrinology* **35**, 347–369 (2014).

71. M. Elderman, P. de Vos, M. Faas, Role of Microbiota in Sexually Dimorphic Immunity. *Front Immunol* **9**, 1018 (2018).

72. J. Kalucka, L. P. M. H. de Rooij, J. Goveia, K. Rohlenova, S. J. Dumas, E. Meta, N. V. Conchinha, F. Taverna, L.-A. Teuwen, K. Veys, M. García-Caballero, S. Khan, V. Geldhof, L. Sokol, R. Chen, L. Treps, M. Borri, P. de Zeeuw, C. Dubois, T. K. Karakach, K. D. Falkenberg, M. Parys, X. Yin, S. Vinckier, Y. Du, R. A. Fenton, L. Schoonjans, M. Dewerchin, G. Eelen, B. Thienpont, L. Lin, L. Bolund, X. Li, Y. Luo, P. Carmeliet, Single-Cell Transcriptome Atlas of Murine Endothelial Cells. *Cell* **180**, 764–779.e20 (2020).

73. S. Heinz, C. Benner, N. Spann, E. Bertolino, Y. C. Lin, P. Laslo, J. X. Cheng, C. Murre, H. Singh, C. K. Glass, Simple combinations of lineage-determining transcription factors prime cis-regulatory elements required for macrophage and B cell identities. *Mol Cell* **38**, 576–589 (2010).

74. J. Palomero, M. C. Vegliante, M. L. Rodríguez, A. Eguileor, G. Castellano, E. Planas-Rigol, P. Jares, I. Ribera-Cortada, M. C. Cid, E. Campo, V. Amador, SOX11 promotes tumor angiogenesis through transcriptional regulation of PDGFA in mantle cell lymphoma. *Blood* **124**, 2235–2247 (2014).

75. A. Orang, B. K. Dredge, C. Y. Liu, J. M. Bracken, C.-H. Chen, L. Sourdin, H. J. Whitfield, R. Lumb, S. T. Boyle, M. J. Davis, M. S. Samuel, P. A. Gregory, Y. Khew-Goodall, G. J. Goodall, K. A. Pillman, C. P. Bracken, Basonuclin-2 regulates extracellular matrix production and degradation. *Life Sci Alliance* **6** (2023).

76. Y. Li, J. Zhang, P. Zhai, C. Hu, J. Suo, J. Wang, C. Liu, Z. Peng, The potential biomarker TIFA regulates pyroptosis in sepsis-induced acute kidney injury. *Int Immunopharmacol* **115**, 109580 (2023).

77. M. D. Robinson, D. J. McCarthy, G. K. Smyth, edgeR: a Bioconductor package for differential expression analysis of digital gene expression data. *Bioinformatics* **26**, 139–140 (2010).

78. S. A. John, J. L. Clements, L. M. Russell, L. A. Garrett-Sinha, Ets-1 regulates plasma cell differentiation by interfering with the activity of the transcription factor Blimp-1. *J Biol Chem* **283**, 951–962 (2008).

79. H. Yamamoto, M. S. Lamphier, T. Fujita, T. Taniguchi, H. Harada, The oncogenic transcription factor IRF-2 possesses a transcriptional repression and a latent activation domain. *Oncogene* **9**, 1423–1428 (1994).

80. H. Cui, S. Banerjee, S. Guo, N. Xie, G. Liu, IFN Regulatory Factor 2 Inhibits Expression of Glycolytic Genes and Lipopolysaccharide-Induced Proinflammatory Responses in Macrophages. *J Immunol* **200**, 3218–3230 (2018).

81. D. J. Hodson, A. L. Shaffer, W. Xiao, G. W. Wright, R. Schmitz, J. D. Phelan, Y. Yang, D. E. Webster, L. Rui, H. Kohlhammer, M. Nakagawa, T. A. Waldmann, L. M. Staudt, Regulation of normal B-cell differentiation and malignant B-cell survival by OCT2. *Proc Natl Acad Sci U S A* **113**, E2039–46 (2016).

82. A. Cui, T. Huang, S. Li, A. Ma, J. L. Pérez, C. Sander, D. B. Keskin, C. J. Wu, E. Fraenkel, N. Hacohen, Dictionary of immune responses to cytokines at single-cell resolution. *Nature* **625**, 377–384 (2024).

83. S. Wang, J. Wang, V. Kumar, J. L. Karnell, B. Naiman, P. S. Gross, S. Rahman, K. Zerrouki, R. Hanna, C. Morehouse, N. Holoweckyj, H. Liu, Z. Manna, R. Goldbach-Mansky, S. Hasni, R. Siegel, M. Sanjuan, K. Streicher, M. P. Cancro, R. Kolbeck, R. Ettinger, IL-21 drives expansion and plasma cell differentiation of autoreactive CD11chiT-bet+ B cells in SLE. *Nature Communications* **9**, 1–14 (2018).

84. M. Terekhova, A. Swain, P. Bohacova, E. Aladyeva, L. Arthur, A. Laha, D. A. Mogilenko, S. Burdess, V. Sukhov, D. Kleverov, B. Echalar, P. Tsurinov, R. Chernyatchik, K. Husarcikova, M. N. Artyomov, Single-cell atlas of healthy human blood unveils age-related loss of NKG2CGZMBCD8 memory T cells and accumulation of type 2 memory T cells. *Immunity* **56**, 2836–2854.e9 (2023).

85. S. Ma, Z. Ji, B. Zhang, L. Geng, Y. Cai, C. Nie, J. Li, Y. Zuo, Y. Sun, G. Xu, B. Liu, J. Ai, F. Liu, L. Zhao, J. Zhang, H. Zhang, S. Sun, H. Huang, Y. Zhang, Y. Ye, Y. Fan, F. Zheng, J. Hu, B. Zhang, J. Li, X. Feng, F. Zhang, Y. Zhuang, T. Li, Y. Yu, Z. Bao, S. Pan, C. Rodriguez Esteban, Z. Liu, H. Deng, F. Wen, M. Song, S. Wang, G. Zhu, J. Yang, T. Jiang, W. Song, J. C. Izpisua Belmonte, J. Qu, W. Zhang, Y. Gu, G.-H. Liu, Spatial transcriptomic landscape unveils immunoglobin-associated senescence as a hallmark of aging. *Cell* **187**, 7025–7044.e34 (2024).

86. L. Duong, F. J. Pixley, D. J. Nelson, C. Jackaman, Aging Leads to Increased Monocytes and Macrophages With Altered CSF-1 Receptor Expression and Earlier Tumor-Associated Macrophage Expansion in Murine Mesothelioma. *Front Aging* **3**, 848925 (2022).

87. F. Angum, T. Khan, J. Kaler, L. Siddiqui, A. Hussain, The Prevalence of Autoimmune Disorders in Women: A Narrative Review. *Cureus* **12**, e8094 (2020).

88. M. K. Desai, R. D. Brinton, Autoimmune Disease in Women: Endocrine Transition and Risk Across the Lifespan. *Front Endocrinol (Lausanne)* **10**, 265 (2019).

89. A. Sziraki, Z. Lu, *Computational Pipeline for Processing EasySci Data* (2023; https://zenodo.org/record/8395492).

90. B. K. Martin, C. Qiu, E. Nichols, M. Phung, R. Green-Gladden, S. Srivatsan, R. Blecher-Gonen, B. J. Beliveau, C. Trapnell, J. Cao, J. Shendure, Optimized single-nucleus transcriptional profiling by combinatorial indexing. *Nat Protoc* **18**, 188–207 (2023).

91. J. Cao, D. R. O'Day, H. A. Pliner, P. D. Kingsley, M. Deng, R. M. Daza, M. A. Zager, K. A. Aldinger, R. Blecher-Gonen, F. Zhang, M. Spielmann, J. Palis, D. Doherty, F. J. Steemers, I. A. Glass, C. Trapnell, J. Shendure, A human cell atlas of fetal gene expression. *Science* **370** (2020).

92. L. McInnes, J. Healy, J. Melville, UMAP: Uniform Manifold Approximation and Projection for Dimension Reduction, *arXiv [stat.ML]* (2018). http://arxiv.org/abs/1802.03426.

93. Y. Hao, S. Hao, E. Andersen-Nissen, W. M. Mauck 3rd, S. Zheng, A. Butler, M. J. Lee, A. J. Wilk, C. Darby, M. Zager, P. Hoffman, M. Stoeckius, E. Papalexi, E. P. Mimitou, J. Jain, A. Srivastava, T. Stuart, L. M. Fleming, B. Yeung, A. J. Rogers, J. M. McElrath, C. A. Blish, R. Gottardo, P. Smibert, R. Satija, Integrated analysis of multimodal single-cell data. *Cell* **184**, 3573–3587.e29 (2021).

94. Y. Zhang, T. Liu, C. A. Meyer, J. Eeckhoute, D. S. Johnson, B. E. Bernstein, C. Nusbaum, R. M. Myers, M. Brown, W. Li, X. S. Liu, Model-based analysis of ChIP-Seq (MACS). *Genome Biol.* **9**, R137 (2008).

95. J. Schug, W.-P. Schuller, C. Kappen, J. M. Salbaum, M. Bucan, C. J. Stoeckert Jr, Promoter features related to tissue specificity as measured by Shannon entropy. *Genome Biol* **6**, R33 (2005).

96. H. K. Finucane, Y. A. Reshef, V. Anttila, K. Slowikowski, A. Gusev, A. Byrnes, S. Gazal, P.-R. Loh, C. Lareau, N. Shoresh, G. Genovese, A. Saunders, E. Macosko, S. Pollack, Brainstorm Consortium, J. R. B. Perry, J. D. Buenrostro, B. E. Bernstein, S. Raychaudhuri, S. McCarroll, B. M. Neale, A. L. Price, Heritability enrichment of specifically expressed genes identifies disease-relevant tissues and cell types. *Nat Genet* **50**, 621–629 (2018).

97. D. A. Cusanovich, A. J. Hill, D. Aghamirzaie, R. M. Daza, H. A. Pliner, J. B. Berletch, G. N. Filippova, X. Huang, L. Christiansen, W. S. DeWitt, C. Lee, S. G. Regalado, D. F. Read, F. J. Steemers, C. M. Disteche, C. Trapnell, J. Shendure, A Single-Cell Atlas of In Vivo Mammalian Chromatin Accessibility. *Cell* **174**, 1309–1324.e18 (2018).

98. E. Sollis, A. Mosaku, A. Abid, A. Buniello, M. Cerezo, L. Gil, T. Groza, O. Güneş, P. Hall, J. Hayhurst, A. Ibrahim, Y. Ji, S. John, E. Lewis, J. A. L. MacArthur, A. McMahon, D. Osumi-Sutherland, K. Panoutsopoulou, Z. Pendlington, S. Ramachandran, R. Stefancsik, J. Stewart, P. Whetzel, R. Wilson, L. Hindorff, F. Cunningham, S. A. Lambert, M. Inouye, H. Parkinson, L. W. Harris, The NHGRI-EBI GWAS Catalog: knowledgebase and deposition resource. *Nucleic Acids Res* **51**, D977–D985 (2023).

99. T. Stuart, A. Srivastava, S. Madad, C. A. Lareau, R. Satija, Single-cell chromatin state analysis with Signac. *Nat Methods* **18**, 1333–1341 (2021).

100. J. A. Castro-Mondragon, R. Riudavets-Puig, I. Rauluseviciute, R. B. Lemma, L. Turchi, R. Blanc-Mathieu, J. Lucas, P. Boddie, A. Khan, N. Manosalva Pérez, O. Fornes, T. Y. Leung, A. Aguirre, F. Hammal, D. Schmelter, D. Baranasic, B. Ballester, A. Sandelin, B. Lenhard, K. Vandepoele, W. W. Wasserman, F. Parcy, A. Mathelier, JASPAR 2022: the 9th release of the open-access database of transcription factor binding profiles. *Nucleic Acids Res* **50**, D165–D173 (2022).

101. Z. Gu, R. Eils, M. Schlesner, Complex heatmaps reveal patterns and correlations in multidimensional genomic data. *Bioinformatics* **32**, 2847–2849 (2016).

7. Z. Zhang, C. Schaefer, W. Jiang, Z. Lu, J. Lee, A. Sziraki, A. Abdulraouf, B. Wick, M. Haeussler, Z. Li, G. Molla, R. Satija, W. Zhou, J. Cao, A panoramic view of cell population dynamics in mammalian aging. Science 387, eadn3949 (2025).